Ore Geology Reviews 72 (2016) 355–372

Contents lists available at ScienceDirect

Ore Geology Reviews

journal homepage: www.elsevier.com/locate/oregeorev

Ore geology and fluid evolution of the giant Caixiashan carbonate-hosted Zn–Pb deposit in the Eastern Tianshan, NW China

Deng-Feng Li [a,b], Hua-Yong Chen [a,*], Li Zhang [a], Pete Hollings [c], Yan-Jing Chen [d], Wan-Jian Lu [a,b], Yi Zheng [e], Cheng-Ming Wang [a,b], Jing Fang [a,b], Gang Chen [f], Gang Zhou [f]

[a] Key Laboratory of Mineralogy and Metallogeny, Chinese Academy of Sciences, Guangzhou 510640, China
[b] Graduate University of Chinese Academy of Sciences, Beijing 100049, China
[c] Department of Geology, Lakehead University, 955 Oliver Road, Thunder Bay, ON P7B 5E1, Canada
[d] Key Laboratory of Crust and Orogen Evolution, Peking University, Beijing 100871, China
[e] Department of Earth Sciences, Sun Yat-sen University, Guangzhou 510472, China
[f] Xinjiang Bureau of Geology and Mineral Resources, Urumqi, Xinjiang 830000, China

ARTICLE INFO

Article history:
Received 6 April 2015
Received in revised form 5 August 2015
Accepted 7 August 2015
Available online 11 August 2015

Keywords:
Carbonate-hosted Zn–Pb deposit
Ore geology
Fluid inclusion
The Eastern Tianshan

ABSTRACT

The Caixiashan giant carbonate-hosted Zn–Pb deposit (~131 Mt@ 3.95% Zn + Pb) formed by replacement of dolomitized marble, with stratiform massive and breccia bodies is located near the base of the Proterozoic Kawabulake Group limestone and marble. It is one of the largest carbonated-hosted massive sulfides Zn–Pb ore deposits in Northwest China to have been discovered in recent years.

Abundant pyrite occurs in dolomitized marble, along fractures in dolomitized clasts in the host rocks and filling cracks in the host rock. Locally, colloform or framboidal pyrites are observed in the early period and sometimes replaced by the later sphalerite. The sulfide assemblage of the main ore stage is characterized by massive or disseminated sphalerite and galena, with less pyrite than the earlier stage, and minor pyrrhotite. Galena occurs as small veins cutting the early-formed sphalerite. Dolomite and calcite are the main gangue minerals that co-precipitated with these sulfides. Tremolite and quartz alteration commonly overprints the orebodies. According to the crosscutting relationships and the different mineral associations within the host rocks and ore bodies, three stages are recognized at Caixiashan, i.e., syn-sedimentary pyrite (stage I), pyrite alteration, sphalerite–carbonate and galena–pyrite–carbonate (stage II-1, stage II-2 and stage II-3, respectively) and magmatic/metamorphic reworking (stage III).

Calcite and quartz crystals are important host minerals among the three hypogene stages (stages I–III, although quartz mainly occurred in stage III). Stage I contains only aqueous inclusions (W-type), which were homogenized from 110 to 236 °C (main range of 138–198 °C and average at 168 °C; main range = average ± σ) and the salinities are from 0.5 to 16.5 (main range of 5.1–15.1 with average of 10.1) wt.% NaCl eqv. In the pyrite alteration of stage II-1 the W-type fluid inclusions homogenized from 175 to 260 °C (main range of 210–260 with average of 235) and the salinities range from 8.5 to 22.4 (main range of 16.7–20.1 with average of 18.4) wt.% NaCl eqv. In the main Zn–Pb mineralization stage (stage II-2–3), four types of fluid inclusions were identified an aqueous phase (W-type), a pure carbon phase (PC-type), a carbon phase containing (C-type) and mineral bearing inclusions (S-type). The W-type fluid inclusions of stage II-2–3 homogenized at 210 to 370 °C (main range of 253–323 and average at 270) and the salinities range from 5.9 to 23.1 (main range of 13.3–20.3 with average at 16.8) wt.% NaCl eqv.; C-type homogenized at 237 °C to 371 °C and the salinities range from 6.4–19.7 wt.% NaCl eqv.; S-type fluid inclusions homogenized at 211 to 350 °C and daughter minerals melted between 340 and 374 °C during heating, indicating a salinity range of 42 to 44 wt.% NaCl eqv. PC-type fluid inclusions with homogenization temperatures of CO_2 phase show large variation from 7.4 °C to 21.2 °C. Laser Raman analyses show that CH_4, CO_2 and SO_4^{2-} coexist in the main mineralization stage fluids. The magmatic/metamorphic reworking stage only contains W-type fluid inclusions which yield homogenized between 220 and 360 °C (main range of 251–325 and average at 288), with salinities ranging from 1.7 to 23.0 (main range of 14.3–20.0 and average at 18.8) wt.% NaCl eqv.

The textural features, mineral assemblages and fluid geochemistry suggest that the Zn–Pb ores were formed through hydrothermal convection of hot marine waters along the faults and fractures resulting in metal (Zn,

* Corresponding author at: Guangzhou Institute of Geochemistry, Chinese Academy of Sciences, P.O. Box 1131, Tianhe District, Guangzhou 510640, Guangdong, China.
E-mail address: huayongchen@gig.ac.cn (H.-Y. Chen).

http://dx.doi.org/10.1016/j.oregeorev.2015.08.007

Pb and Fe) enriched stratiform orebodies. Subsequent rapid precipitation of sulfides was triggered by sulfate (SO_4^{2-}) thermal reduction with the CH_4 preserved in sedimentary rocks and early stage I pyrite bodies. This process occurred at moderate temperatures (*ca.* 270 °C). Higher-temperature magmatic hydrothermal alteration overprinted the orebodies, but only provided a minor contribution to the mineralization.

1. Introduction

Carbonate-hosted Zn–Pb deposits play a significant role in the world's supply of Pb and Zn (Kucha et al., 2010; Leach et al., 2005). The Caixiashan Zn–Pb deposit is one of the largest carbonate-hosted Zn–Pb ore deposits in the Eastern Tianshan Terrane, NW China (Fig. 1). Mining of the Caixiashan deposit has focused on four major areas, namely Zones I to IV. Exploration began in 2002, and production commenced two years later. The Caixiashan Zn–Pb deposit has current reserves of 131 Mt at 3.95% Pb + Zn (Zn > Pb; cut off by 0.5% Pb + Zn; Cao et al., 2013).

Some aspects of the Caixiashan Zn–Pb deposit including the major and trace element geochemistry of the host rocks (Liang et al., 2008; Peng et al., 2007), the general isotope compositions and the fluid inclusion studies were initially constrained. Whole rock sulfur isotopes range from −21.1 to 19.1‰ with the majority of the values being positive whereas carbon and oxygen isotopic compositions range from −2.4 to 0.1‰ and 5.9 to 19.1‰, respectively (Cao et al., 2013; Gao et al., 2007). Published fluid inclusion homogenization temperatures vary from 180 °C to 310 °C with salinity range from 1.4 to 23.1 wt.% NaCl eqv. (Gao et al., 2006) or homogenized at 190 °C to 240 °C with salinity range from 0 to 6.0 wt.% NaCl eqv. (Sun et al., 2013). However, these results were not constrained by detailed paragenetic studies as the detailed geology, especially the paragenetic relationships of mineralization and alteration, and the corresponding ore forming processes of Caixiashan are poorly understood. One of the most commonly discussed but least well-understood aspects of the deposit is the source of the ore-forming fluid with previous studies proposing either magmatic hydrothermal fluids (Cao et al., 2013) or sedimentary brines (Peng et al., 2008). Other aspects that still remain controversial include the pressure, volume and temperature (*PVT*) variations of ore-forming fluids from the multiple paragenetic stages, the precipitation mechanism of metals and the preservation regime of ore bodies. These parameters are critical to defining the metallogenesis of carbonated-hosted deposits (Appold and Wenz, 2011).

To help clarify these questions, this paper characterizes the ore petrology and ore-forming fluids in the various paragenetic stages present in the Caixiashan deposit. We provide a detailed documentation of the temporal and spatial evolution of the mineralizing system for this newly discovered giant Zn–Pb deposit in NW China. Based on this information, the mechanisms that control the precipitation of Zn and Pb sulfides and the genetic link between dolomite and tremolite alteration and mineralization will be discussed.

2. Regional geology

The Caixiashan Zn–Pb mining district is located between the Central Asian Orogenic Belt (CAOB) and Tarim (Fig. 1A), and hosted in the northern margin of the Central Tianshan Terrane, about 200 km south of Hami city in the Xinjiang Uygur Autonomous Region, NW China. The Central Tianshan Terrane is located in the southern part of the Eastern Tianshan, between the Junggar Basin in the north and Tarim Basin in the south (Fig. 1B). The Eastern Tianshan was affected by the collision of the Junggar and the Tarim plates during the Ordovician to the Carboniferous (Allen and Natal'in, 1995; Pirajno et al., 2008) and is usually classified into four parts from north to south, i.e., Dananhu–tousuquan, Kanggurtag–huangshan shear zone, Aqishan–Yamansu volcanic belt and Central Tianshan Terrane, separated by a series of E-trending faults from north to south, including the Kanggurtag, Yamansu, Aqikekuduke and Tuokexun faults (Fig. 1C).

The Caixiashan Zn–Pb deposit is hosted in Precambrian platform carbonates of the Kawabulake Group. Smaller Pb–Zn deposits such as the Jiyuan, Hongxishan, Hongyuan and Shaquanzi occur in the same rocks in the eastern section of the Central Tianshan Terrane. The Mesoproterozoic Kawabulake Group is well exposed in the Central Tianshan Terrane and located in the area south of Aqikekuduke Fault and northeast of Tuokexun Fault (Fig. 1C), unconformably overlain by the Lower Cambrian Huangshan Formation (fault contact with mid-Carboniferous Matoutan Formation in the study area) and conformably underlain by the Mesoproterozoic Xingxingxia Group in the Eastern Tianshan area (Cai et al., 2013; Xiu et al., 2002). The depositional age of the Kawabulake Group is therefore after the Xingxingxia Group but before the Lower Cambrian Huangshan Formation, as confirmed by the occurrence of stromatolite (e.g., *Conophyton cylindrical*; Dong, 2005) and a single zircon grain U–Pb age of 1141 ± 60 Ma (Xiu et al., 2002). The brief outline given here is largely based on the previous studies (Cai et al., 2013; and references therein). The Kawabulake Group is comprised of two lithologic sections (Fig. 2), from bottom to top: the basal unit (section I) comprises siltstones with chert interlayers overlain by slate with siliceous rock interlayers and sandstone lenses, followed by sandstone and slate with quartz veins and capped by slate after a layer of siltstone. Section II comprises a basal package of sandstone with dolomitized marble overlain by a narrow carbon-bearing-shale within the siliceous rock layer conformably roofed by a massive layer of sandstone, then a very thin layer of carboniferous shale with siltstone lenses capped by a phyllite interbedded with siltstone and chert, among which there are some small layers of carbon-bearing-shale, chert and andesite (Fig. 2). The formation of a carbonate platform suggests that the Eastern Tianshan formed in a stable sedimentary environment during the Precambrian (Cai et al., 2013).

Combined with the available geochemical and chronological data from the Central Tianshan Terrane and the Tarim Craton (Cai et al., 2013; Xia et al., 2012), the subduction and accretion processes of the Tarim Craton and Tianshan area are described as below: (1) from the Mesoproterozoic to Middle Neoproterozoic, a continental rift or a passive continental margin formed at the northern margin of the Tarim, accompanied by an ancient ocean basin (proto-Paleoasian Ocean) formed at least before 890 Ma (Zheng et al., 2010). During that time the basement of the Central Tianshan Terrane was formed along passive continental margins. (2) The Central Tianshan Terrane drifted northwards to the active southern margin of the Siberian Craton in the Late Paleozoic; resulting in the termination of the Paleoasian Ocean during the Late Carboniferous and Permian (Xiao et al., 2009). The presence of high-Mg diorite and adakite in the northern and southern margins of the Central Tianshan Terrane suggests the closure of the Northern and Southern Tianshan Ocean (Tang et al., 2012; Yin et al., 2010). (3) The overlapping of the plates eventually led to the initiation of subduction on both the northern and southern margins of the Central Tianshan Terrane no later than ~350 Ma, forming active arcs and back (intra)-arc systems (Xiao et al., 2009).

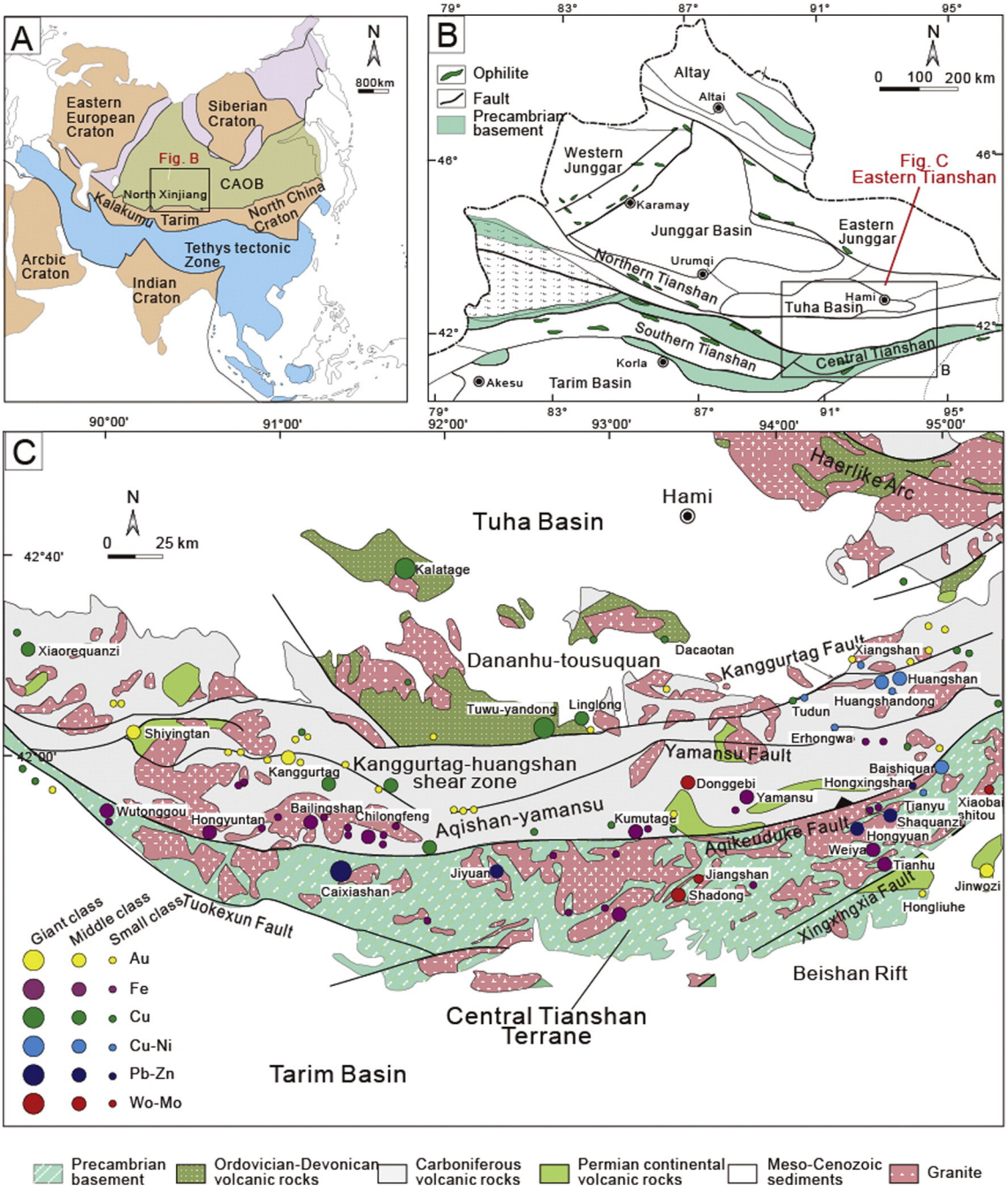

Fig. 1. Geological map showing the main units in the Eastern Tianshan area and location of the Caixiashan carbonate-hosted Zn–Pb deposit in the Kawabulake Group. A, location of the Central Asian Orogenic Belt and Tarim. B, location of the Eastern Tianshan. C, location and major tectonic units in the Eastern Tianshan.
Modified after Deng et al. (2014).

3. Geology of the Caixiashan ore deposit

3.1. Deposit geology

The local stratigraphy in the Caixiashan area was described by Cai et al. (2013) and the geology in the mining district is summarized in Fig. 2. The ore minerals of the ore bodies are comprised predominantly of sphalerite and pyrite, with lesser galena and pyrrhotite, and minor arsenopyrite. The majority of in the Caixiashan field occurs in four high-grade ore zones (at a 0.5% Pb + Zn cut-off), namely Zones I, II, III and IV (Fig. 3). Zone I strikes 078° and dips 80° to south with an outcrop around 6–210 m wide and 1000 m long, Zone II strikes 075° and dips 70°–75° to south with an outcrop around 100–350 m wide and 1300 m long, Zone III strikes 078° and dips 65°–75° to south with an outcrop around 100–350 m wide and 500 m long, and Zone IV strikes 090° and dips 70° to south with an outcrop around 200 m wide and 900 m long (Fig. 3). The Caixiashan Zn–Pb mining district currently contains reserves of 131 Mt at 3.95% Pb + Zn (Zn > Pb; cut-off by 0.5% Pb + Zn; Cao et al., 2013). The ore bodies of the Caixiashan district mainly occur in dolomite/dolomitic-marble or in the contact zone of dolomitic marble with the platform carbonates of the Mesoproterozoic Kawabulake Group and are broadly distributed as massive, layers, disseminated or veinlets.

The Caixiashan Zn–Pb deposit is localized by at least three episodes of faulting, the earliest episode includes normal faults formed slightly before/during mineralization, with similar strike and dip

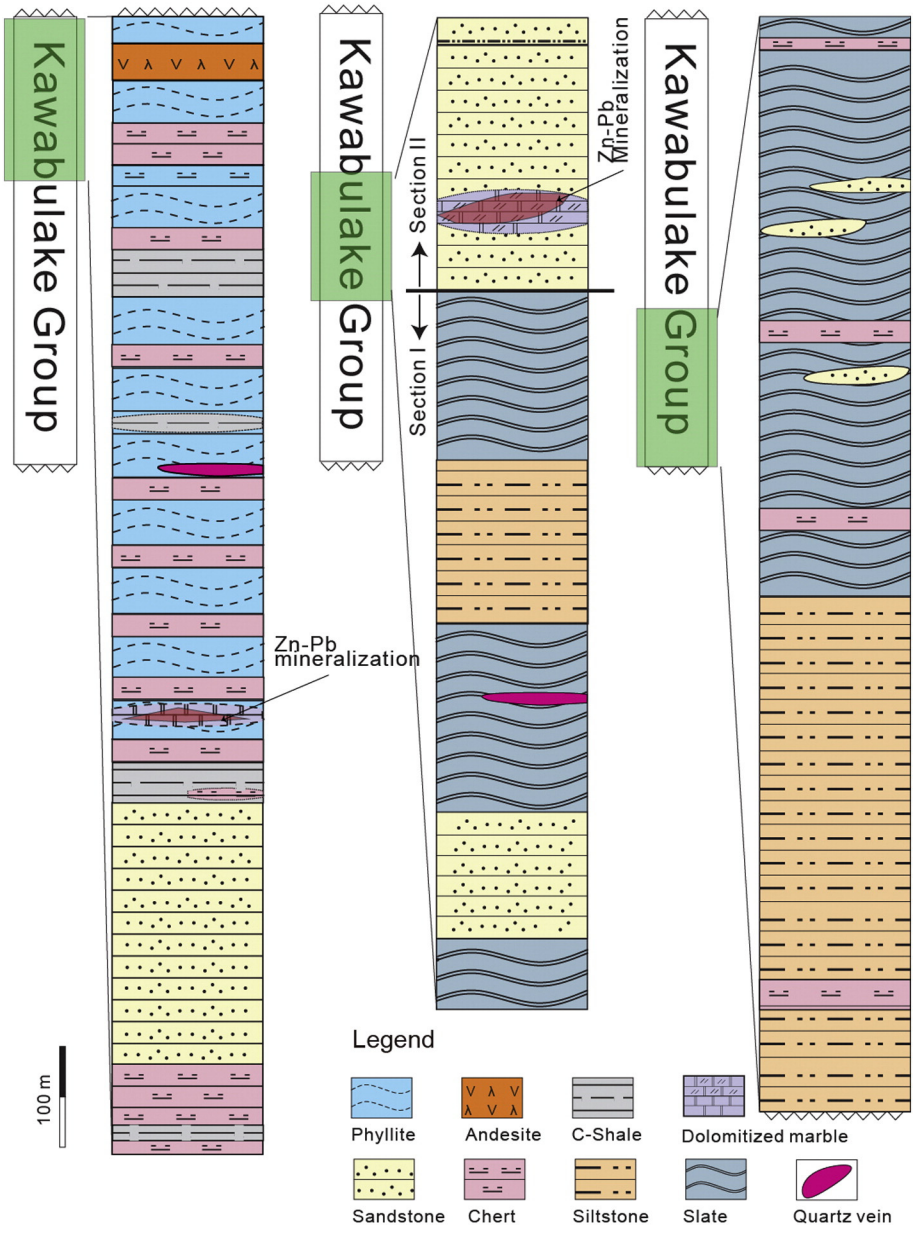

Fig. 2. Generalized stratigraphic columns of the Mesoproterozoic Kawabulake Group.

(dips 70°–80° to the south) to the bedding, and occurs mostly toward the basin, indicated that these faults are synsedimentary and control the sedimentation of the Kawabulake Group (F1; Fig. 3). The second episode comprises northeast-trending normal faults which control the high grade ore Zones I and IV (F2; Fig. 3). The third episode comprises faults that cross cut those of the second episode, which are restricted to the main deposit and usually cut the ore body and host rock (F3; Fig. 3).

Magmatism in the mining area shows no clear spatial relationship to mineralization with many of the magmatic rocks in the mining area having formed between 350–320 Ma (Gao et al., 2006). Numerous diorite dikes were emplaced along fractures and crosscut the ore bodies, which decreases the ore grade and generated variable degrees of tremolite and silica alteration in the wall rock. The Mesoproterozoic carbonate rocks have been locally metamorphosed to greenschist facies during the Paleozoic with dynamic metamorphism having generated mylonites along the faults.

Obvious open-space filling of voids, brecciation and replacement of the host rocks can be observed in drill core, hand specimens and thin sections. The sedimentary fragments are cemented by calcite, quartz and/or sulfides consistent with epigenetic hydrothermal processes. The wall rock alteration in the Caixiashan mining district includes the following minerals: dolomite, quartz and tremolite. Dolomitic alteration is the most important which occurs in both footwall and hanging-wall rocks. There is a close association between sulfides and dolomitized marble (Fig. 4), and the sulfides commonly occur as disseminations and veinlets within the dolomite. Dolomite generally occurs either as fine-grained crystals in the rock matrix or medium- to coarse-grained euhedral crystals.

The mineral assemblage of the main mineralizing stage in the Caixiashan deposit is relatively simple and the principal economic ore mineral is sphalerite with lesser galena. Other minor minerals include pyrite, pyrrhotite, arsenopyrite with trace chalcopyrite, kilbrickenite ($Pb_9Sb_{22}S_{42}$, identified by X-ray scattering techniques), tetrahedrite ($Cu_{12}Sb_4S_{13}$), boulangerite ($Pb_5Sb_4S_{11}$), bournonite ($CuPbSbS_3$) and pyrargyrite (Ag_3SbS_3; Liang et al., 2008). The gangue minerals are mainly dolomite, calcite and tremolite, minor quartz.

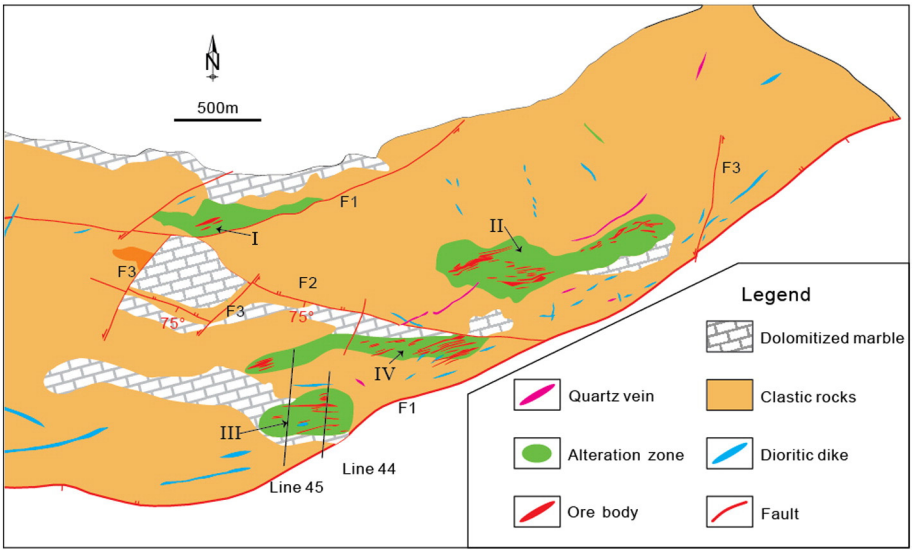

Fig. 3. Geological map of the Caixiashan Zn–Pb deposit.
Modified after Peng et al. (2007).

3.2. Paragenetic sequences of mineralization and alteration

Forty-nine polished thin sections of representative ore samples were observed using a polarizing microscope. Based on the cross-cutting relationships and mineral assemblages identified within the deposit, the mineralizing process of the Caixiashan can be divided into three stages, as follows: stage I is characterized by syn-sedimentary pyrite (Fig. 5A–D); stage II-1 with pyrite-alteration (Fig. 5E–G), sphalerite–carbonate (stage II-2; Fig. 6), galena–pyrite–carbonate (stage II-3; Fig. 7); and a stage III of

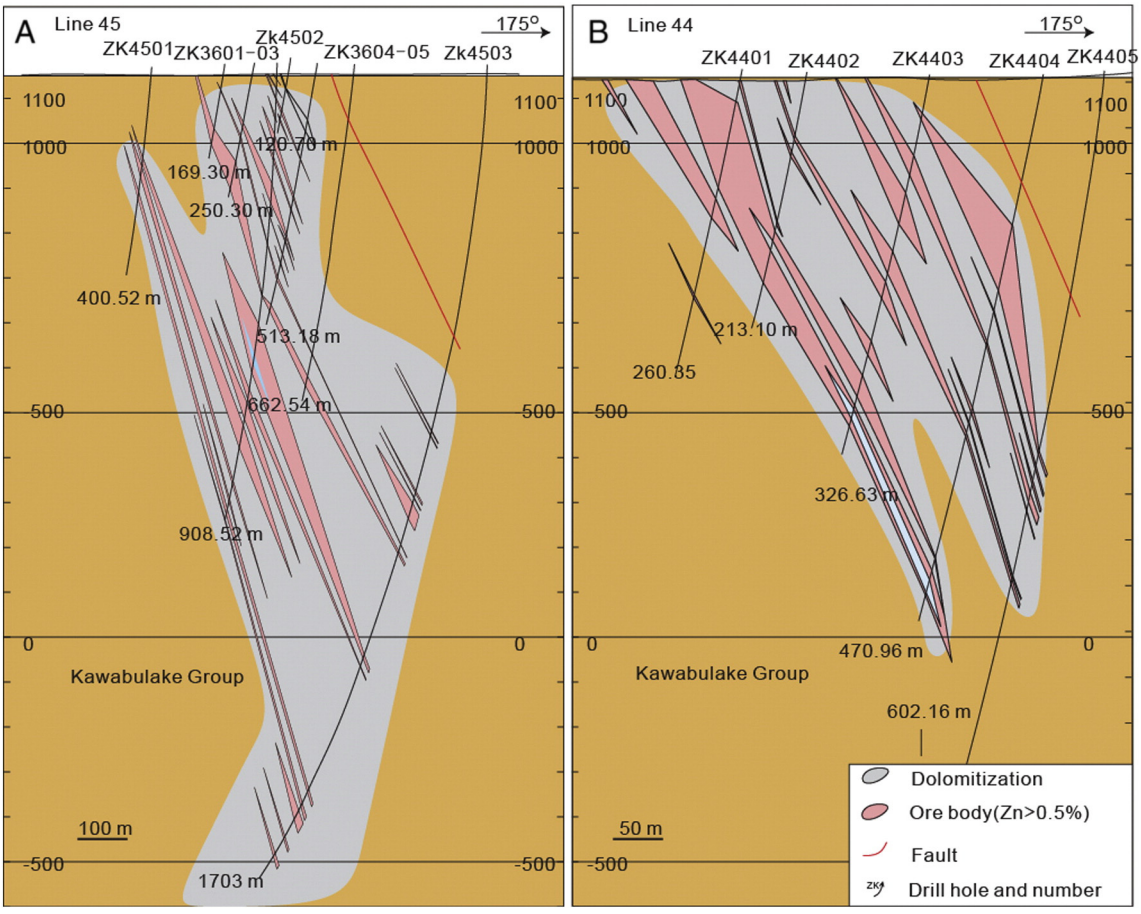

Fig. 4. Cross section of the Caixiashan Zn-Pb deposit along lines 44 and 45 of Fig. 3, showing the location and the depth of the drill holes.
Modified after Geological Team 1 of Xinjiang Bureau of Geology and Mineral Resources (2007).

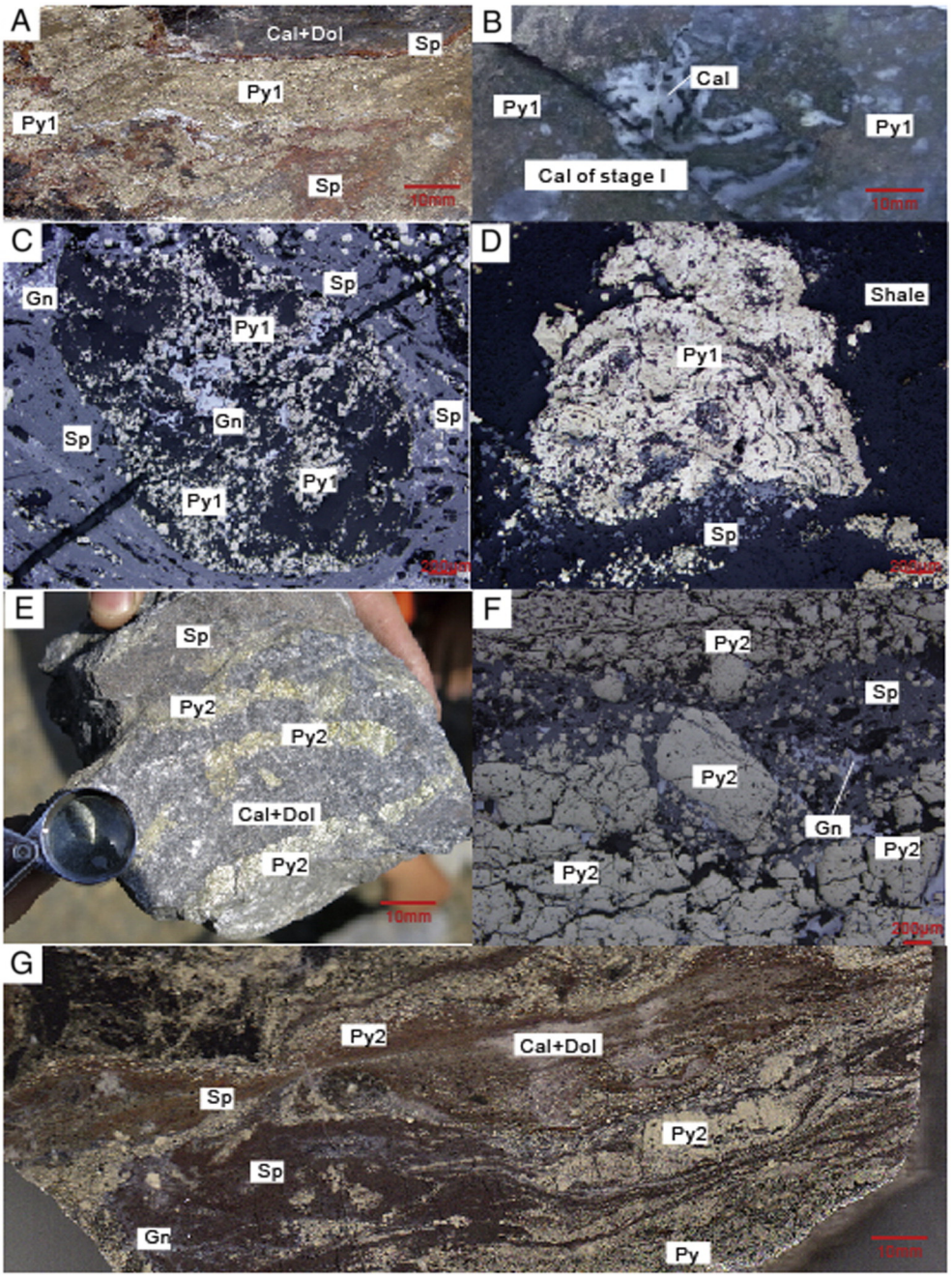

Fig. 5. Core and hand specimen photographs and reflected light photomicrographs of stage I (A–D: pyrite 1) and stage II-1 (E–G: pyrite 2). A, massive pyrite (pyrite 1) with dolomite and calcite, there are some sphalerite veins of stage II crosscutting the pyrite. Sample 13ZK1603-4, Zone I. B, cross section of pyrite (pyrite 1) enclosing the dolomite and calcite. Sample 13CXS-34, Zone II. C, framboidal pyrite (pyrite 1) replaced by the sphalerite. Sample 13CXSIII-15, Zone III. D, colloform crystals of pyrite (pyrite 1) was replaced by sphalerite. Sample IZK1603-3/46 m, IZK1603. E, layered pyrite (pyrite 2) interbedded with calcite and dolomite, some stage II-2 sphalerite around the corner. Sample 13CXS-34, Zone II. F, pyrite 2 replaced by the sphalerite/galena. Sample 13CXS-15, Zone I. G, vein type sphalerite, galena, calcite and dolomite crosscutting the pyrite 2, Sample 13CXS-44, Zone I. Abbreviations: Py = pyrite; Sp = sphalerite, Dol = dolomite, Cal = calcite, Gn = galena, Po = pyrrhotite, Qtz = quartz, Tr = tremolite, Apy = arsenopyrite.

magmatic/metamorphic reworking (Fig. 8). The mineral paragenetic sequences are illustrated in Fig. 9.

3.2.1. The syn-sedimentary pyrite stage

Three fundamental minerals comprise stage I, i.e., pyrite, dolomite and calcite. The massive pyrite (pyrite 1) is hosted in the limestone and some of them were replaced by tiny sphalerite veins (Fig. 5A), or coexist with calcite and dolomite (Fig. 5B) containing numerous fluid inclusions. The massive pyrite shows typical framboidal (Fig. 5C) and colloform (Fig. 5D) textures in thin section. The framboidal pyrite is composed of tiny pieces of anhedral pyrite and locally enclosed by the fine-grained sphalerite (Fig. 5C). The presence of colloform pyrite reflects rapid crystallization on the seafloor caused by mixing of ascending hydrothermal fluids with cold ambient seawater (Herzig and Hannington, 1995). Pyrite 1 locally shows pseudomorphous replacement of colloform pyrite by sphalerite (stage II-2) with preservation of the original texture.

3.2.2. The pyrite–sphalerite–galena–carbonate stage

Stage II can be divided into three sub-stages from early to late, i.e., pyrite-alteration (stage II-1), sphalerite–carbonate (stage II-2) and galena–pyrite–carbonate stages (stage II-3). Stage II-1 pyrite (pyrite 2) commonly occurs as layers in the matrix made up of recrystallized calcite and dolomite with medium grain size (Fig. 5E). The uniform

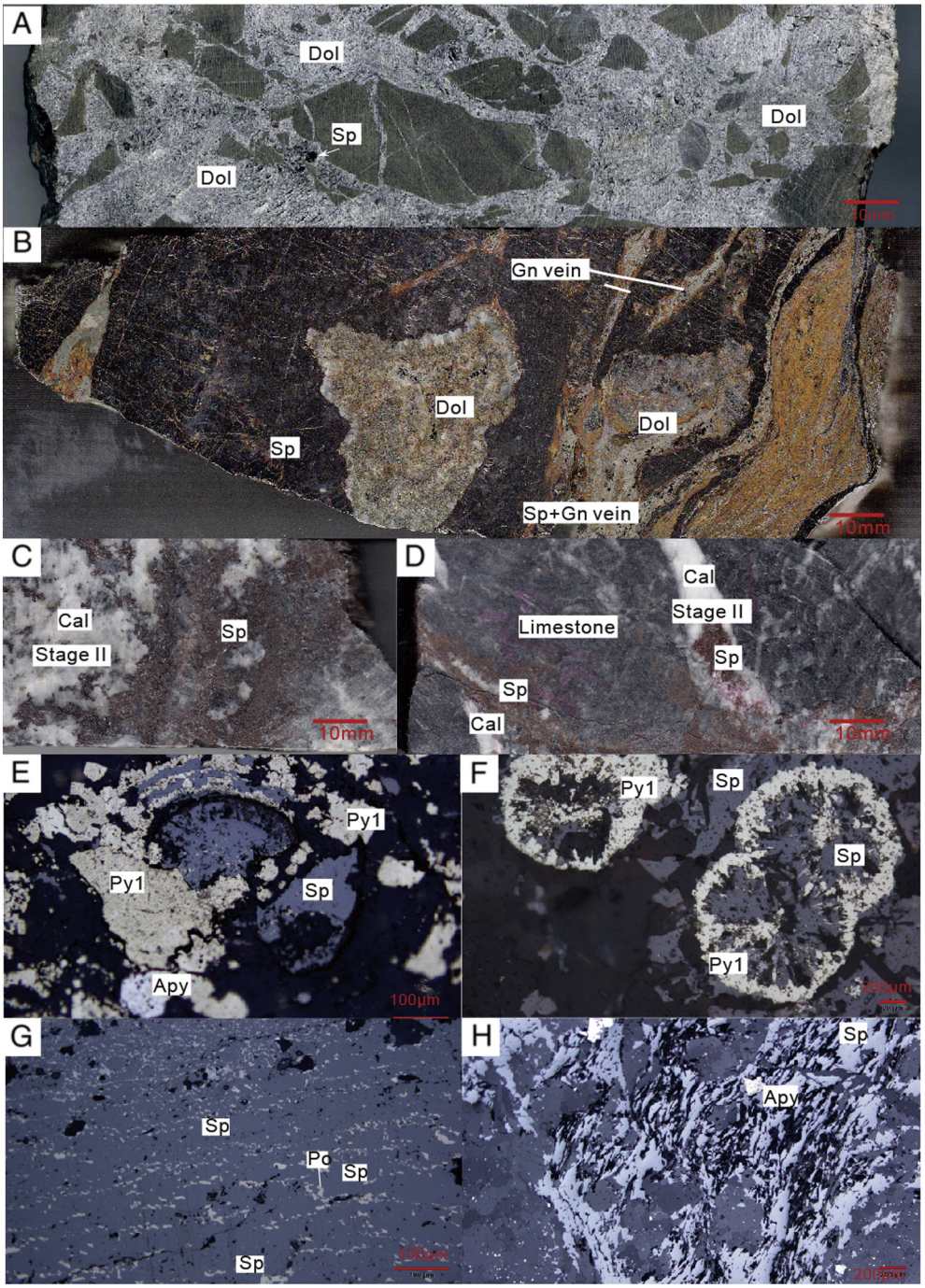

Fig. 6. Core and hand specimen photographs of the sphalerite-carbonate (stage II-2) stage. A, dolomite preferentially replacing the matrix of typical host rock breccia. Sample 371/371 m, IIZK4701. B, massive crystals of sphalerite with dolomite core and crosscut by narrow galena veins. Sample 13CXS-21, Zone II. C, disseminated sphalerite and galena co-precipitated with calcite. Sample 13ZKII-C8, ZK4701 of Zone II. D, sphalerite occurs in the calcite vein. Sample 13ZKII-C15, ZK4701 of Zone II. E, sphalerite replaced colloform pyrite (pyrite 1) while preserving the colloform texture of pyrite. Sample IZK1603-2/74 m, IZK1603. F, sphalerite replaced subhedral pyrite (pyrite 1) from the core to the rim. Sample 12CXS-2–4, Zone II. G, massive sphalerite contains tiny pyrrhotite showing exsolution texture. Sample 13CXSIII-15, Zone III. H, the sphalerite shows deformation textures. Sample 13CXIII-61, Zone III. Abbreviations: Py = pyrite; Sp = sphalerite, Dol = dolomite, Cal = calcite, Gn = galena, Po = pyrrhotite, Qtz = quartz, Tr = tremolite, Apy = arsenopyrite.

layered pyrite 2 with medium-grained calcite and dolomite suggests the pyrite formed simultaneously with the recrystallized carbonates, which is distinct from stage I sedimentary pyrite 1 with diagnostic colloform or framboidal textures. Based on the close association between layered pyrite and sphalerite orebodies, pyrite 2 has been assigned to stage II-1 to distinguish it from stage I pyrite 1. Pyrite 2 is also locally replaced by small amounts of sphalerite of stage II-2 as well as narrow galena veins (Fig. 5F): some of the veins (sphalerite/galena) occur between the pyrite layers whereas others cut those layers (Fig. 5G).

The host rock clasts are cemented by dolomite + sphalerite (Fig. 6A). Stage II-2 is characterized by abundant massive sphalerite co-precipitated with medium-grained subhedral to euhedral dolomite and calcite (Fig. 6B), followed by some disseminated sphalerite coexisting with calcite veins (Fig. 6C), which locally crosscut the host limestone (Fig. 6E). As with stage I, stage II-2 sphalerite replaces the stage I massive pyrite (pyrite 1; Figs. 5A, 6E and F). Some of the massive sphalerite ore contains minor pyrrhotite as small grains with linear distribution showing possible exsolution textures, suggesting that the pyrrhotite probably

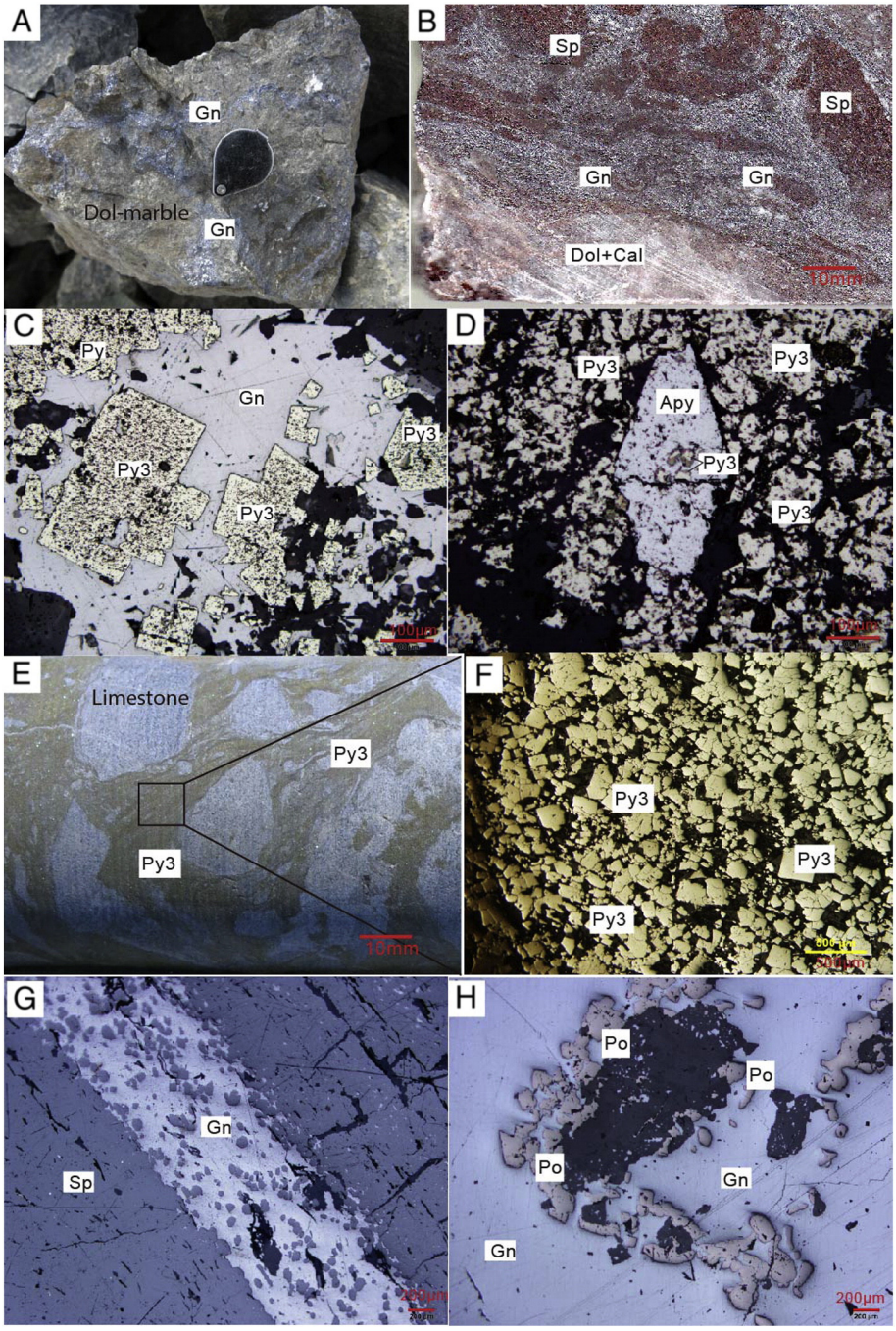

Fig. 7. Core and hand specimen photographs of the galena–pyrite–carbonate (stage II-3; pyrite 3) stage. A, the hand sample shows the galena veins cutting the dolomitized marble. Sample 13CXSIV-3, Zone 4. B, drill core section shows the s the galena vein cut the sphalerite. Sample II0031038-4/1120 m. ZKII0031038. C, galena coexists with the pyrite (pyrite 3). Sample 13CXSI-01, Zone I. D, euhedral arsenopyrite occurs in the host rock or replaced by pyrite (pyrite 3). Sample 251.71/251 m, ZK4701 of Zone IV. E, collapse texture of pyrite 3 showing the limestone breccia was cemented by pyrite 3. Sample 13ZK4701-17/788 m. ZK4701. F, the thin section shows the pyrite 3 is commonly granular and coarse-grained that cemented the limestone. Sample 13ZK4701-17/788 m. ZK4701. G, massive sphalerite crosscut by galena. Sample II0031038-2/1100 m. ZKII0031038. H, the anhedral pyrrhotite enclosed by the galena. Sample 13CXSIII-11-3. Zone III. Abbreviations: Py = pyrite; Sp = sphalerite, Dol = dolomite, Cal = calcite, Gn = galena, Po = pyrrhotite, Qtz = quartz, Tr = tremolite, Apy = arsenopyrite.

co-precipitated with the massive sphalerite (Fig. 6G). The main stage sphalerite also locally coexists with arsenopyrite (Fig. 6H).

Stage II-3 is dominated by abundant fine-grained galena occurring as small veins cutting across the host rock of dolomitized marble (Fig. 7A), or locally cutting the earlier massive sphalerite ore (Fig. 7B). The galena commonly has sharp boundaries with, but locally replacing granular pyrite (pyrite 3) (Fig. 7C), indicating that the galena probably precipitated slightly later than the Py3. The early stage II arsenopyrite occurs both in the host rock and pyrite 3 partially replacing the pyrite, indicating that the arsenopyrite formed before pyrite 3 (Fig. 7D). The obvious collapse texture between the late pyrite (pyrite 3) and host rock limestone shows the brecciated limestone is cemented by the pyrite 3 (Fig. 7E) or by calcite/dolomite. Pyrite 3 here is commonly granular and coarse-grained (Fig. 7F), distinguishing it from pyrites 1 and 2. Galena usually occurs as anhedral grains, veinlets in a carbonate matrix or crosscutting the sphalerite (Fig. 7G). In Fig. 7H, some pyrrhotites are enclosed by massive galena, which suggests that the pyrrhotite may form a little earlier than the galena, which is consistent with the observation of

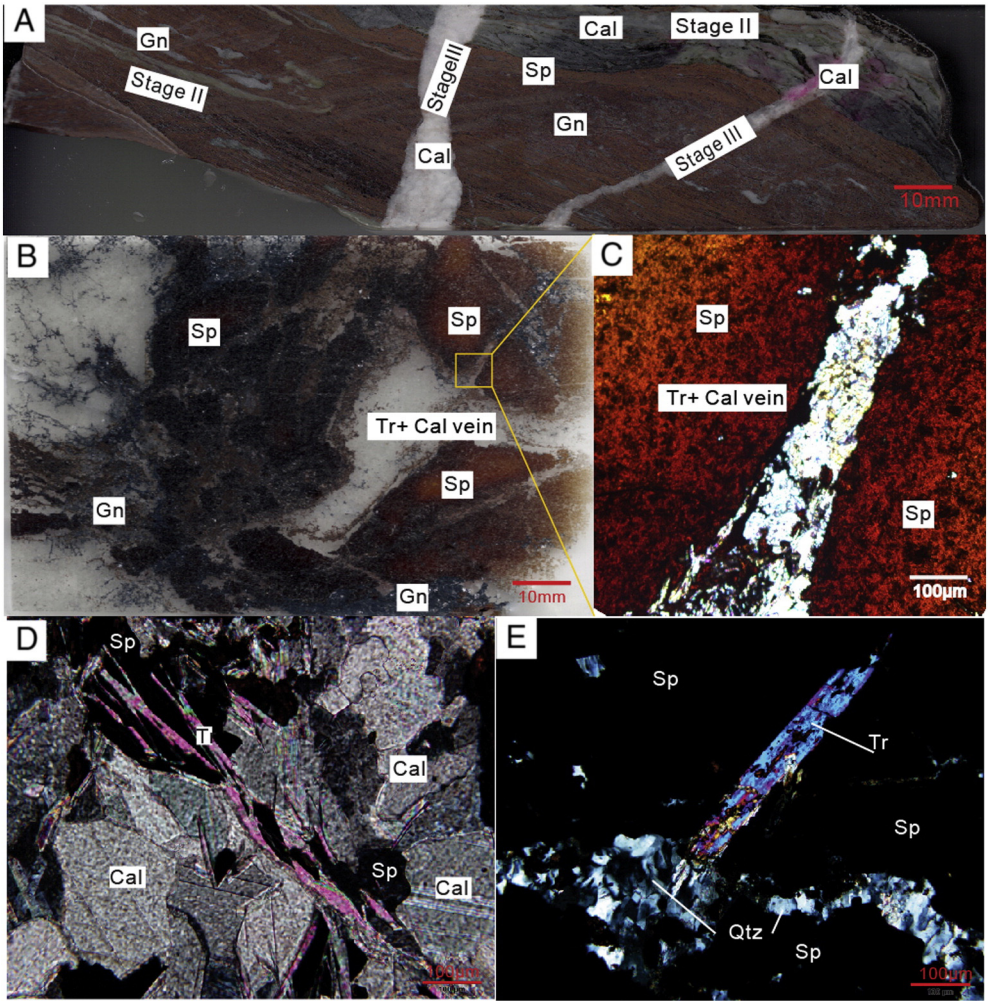

Fig. 8. Core samples and thin sections of magmatic/metamorphic reworking and the supergene stages. A, calcite vein cut across the massive sphalerite. Sample 13ZKIV-91, ZK2901 of Zone IV. B, sphalerite replaced by the tremolite and calcite vein, also noted that the galena cut the sphalerite. Sample 13IVZK2901-562/562 m. ZK2901 of Zone IV. C, close up of the tremolite and calcite veins. Sample 13IVZK2901-562/562 m. ZK2901 of Zone IV. D, sphalerite and dolomite/calcite cut by tremolite. Sample 751/751 m, ZK4701 of Zone IV. E, quartz crosscuts the sphalerite, and both were cut by tremolite. Sample 251.71/251 m, ZK4701 of Zone IV. Zone I. Abbreviations: Py = pyrite; Sp = sphalerite, Dol = dolomite, Cal = calcite, Gn = galena, Po = pyrrhotite, Qtz = quartz, Tr = tremolite, Apy = arsenopyrite.

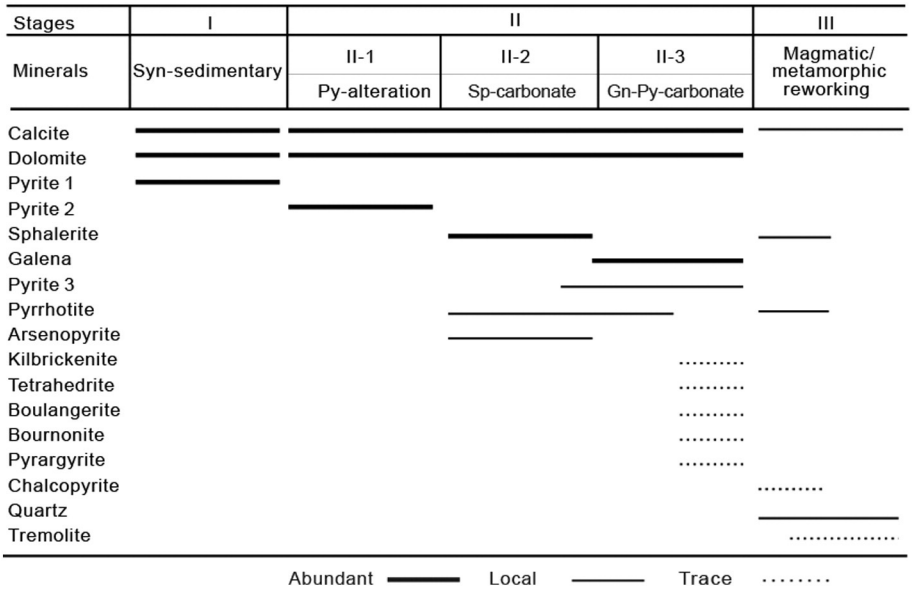

Fig. 9. Mineral paragenesis of the Caixiashan deposit.

coexisting sphalerite and pyrrhotite. Meanwhile, abundant medium- to coarse-grained dolomite and calcite precipitated during formation of galena and pyrite 3. Trace Pb-bearing minerals such as kilbrickenite, tetrahedrite, boulangerite, bournonite and pyrargyrite are also present in this stage.

3.2.3. The magmatic/metamorphic reworking stage

Stage III magmatism-hydrothermal reworking at Caixiashan is made up of tremolite + quartz + calcite, with local sphalerite + quartz, and trace pyrrhotite and chalcopyrite. The fine-grained calcite in stage III occurs as veins crosscutting the massive sphalerite as well as the calcite veins of stage II (Fig. 8A). The tremolite occurs as veins cutting across sphalerite and coexists with some subhedral coarse-grained calcite (Fig. 8B and C), but locally tremolite veins cut the stage II calcite and sphalerite (Fig. 8D). Some fractures are filled with quartz that occurs as chalcedony or fine- to medium-grained, anhedral to subhedral crystals with wavy extinction, and locally coexists with euhedral tremolite (Fig. 8E).

4. Fluid inclusion studies

4.1. Methodology

Calcite, quartz and sphalerite samples of different mineralization stages (stage I: calcite; stage II: calcite with a few sphalerite; stage III: quartz/calcite) were collected from outcrops and drill core from all major orebodies and prepared as doubly polished sections. Hundreds of fluid inclusions in 20 selected thin sections from stages I to III were identified for fluid inclusion petrography and microthermometry.

Fluid inclusion microthermometry was undertaken at the Institute of Geology and Geophysics, Chinese Academy of Sciences (IGGCAS), Beijing, using a Linkam THMSG600 and THMSG1500 freezing and heating system, with a German Zeiss microscope. A U.S. Fluid INC standard was used to correct the temperatures at −56.6 °C, 0.0 °C and 374.1 °C. Fluid inclusions were initially cooled to −190 °C at the rate of −5 °C/min and held for 5 min to make sure all the components in the inclusion were frozen. The inclusion was then warmed at a rate of 5 °C/min and decreased to 0.5 °C/min from −190 to −182.5 °C and −60 to −56.6 °C for the triple point of CH_4 and CO_2, respectively, and held for 1 min in each range. The heating rate was decreased to 1 °C/min from −40 to 30 °C to measure the final melting temperature of CO_2–H_2O clathrate, the partial homogenization temperature of CO_2 and the final melting temperature of ice. Finally, the system was heated at a rate of 3 °C/min until close to the homogeneous phase transition point at which time a lower rate of about 0.5 to 1 °C/min was used.

The fluid inclusion study is based on fluid inclusion assemblages (FIAs). Salinities of aqueous inclusions were calculated using the equation of Bodnar (1993) for the NaCl–H_2O system. Salinities of halite daughter mineral-bearing inclusions were determined using the reference data and methodology of Vityk et al. (1994). Salinities of CO_2-rich inclusions were calculated using the equations of Collins (1979) for the CO_2–NaCl–H_2O system.

Vapor and liquid compositions were measured at the Raman Spectroscopy Laboratory of the Institute of Geology and Geophysics, Chinese Academy of Sciences (IGGCAS), Beijing. An excitation wavelength of 532 nm was used with the Ar^+ ion laser operating at 44 mW. The spectra were measured with 3 second counting times and counted every 1 cm^{-1} from 500 to 4000 cm^{-1}. The laser beam had a spot size of approximately 1 μm with spectral resolution of 0.65 cm^{-1}. It was calibrated on pure silicon produced in France with standard Raman shift of 520.7 cm^{-1}. For peak standards such as CO_2, CH_4 and N_2 see Frezzotti et al. (2012).

4.2. Classification of fluid inclusions

Fluid inclusion types are identified based on their compositions and phases (L–V–S) at room temperatures (~26 °C), and phase transformations during cooling and heating processes (Chen et al., 2007; Goldstein and Reynolds, 1994). Four types of inclusions were identified and designated as W-, C-, PC-, and S- types.

4.2.1. W-type—aqueous fluid inclusions

The W-type inclusions are the most common and show one or two visible phases (liquid H_2O or liquid H_2O and vapor H_2O), with the gas bubble making up approximately 20% to 30% of the entire volume. A few single phase W-type fluid inclusions were found in stage II sphalerite (Fig. 10A). The majority of W-type fluid inclusions have irregular shapes with sizes ranging from 6 to 20 μm (Fig. 10B and C).

4.2.2. C-type—carbon phase fluid inclusions

The C-type inclusions in the calcite are two-phase (vapor CO_2/CH_4 + liquid H_2O) or three-phase (vapor CO_2/CH_4 + liquid CO_2/CH_4 + liquid H_2O), with the gas phase ratio generally in the range of 50%–80% at the start of the cooling process. The CO_2 dominant inclusions are termed C1 whereas the CH_4 dominant inclusions are termed C2 (identified by laser Raman analysis, see below). They are found in stage II-2–3 calcite grains or veins, in groups or as single inclusions (Fig. 10D–F). They are generally triangular or elongate in shape, with sizes ranging from 5 to 23 μm.

4.2.3. PC-type—pure carbon phase fluid inclusions

The PC-type inclusions are $CO_2 \pm CH_4$ (PC1) or pure CH_4 inclusions (PC2), consisting of only a vapor phase at room temperature (Fig. 10F). These inclusions are generally 4 to 23 μm in diameter and rounded isometric or negative crystal in shape.

4.2.4. S-type—the mineral bearing fluid inclusions

The S-type inclusions usually contain at least one daughter mineral (Fig. 10G–I), and show rounded, elliptical and negative shapes with the longest dimensions ranging from 4 to 16 μm. Their vapor bubbles can be either CH_4/CO_2 or H_2O, and occupy 5–20% of the total volume. The majority of cubic minerals in the S-type inclusions are halite.

4.3. Microthermometry results

All the identified fluid inclusions in calcite and quartz crystals from multiple paragenetic stages were analyzed and their microthermometric results are presented in Table 1 and Fig. 11.

The stage I calcite contains only W-type fluid inclusions, which yield final ice-melting temperatures of −12.6 to −0.3 °C (around −16.7 to −12.7 °C) with an average of −14.7 °C, constraining a salinity range of 0.5 to 16.5 (around 5.1 to 15.1) wt.% NaCl eqv. with an average of 10.1 wt.% NaCl eqv. They were homogenized to liquid at 110 to 236 °C (around 138 to 198 °C) at an average of 168 °C. Based on the Tm_{ice} and Th_{-tal} of the W-type fluid inclusions, the estimated fluid density is 0.85 to 1.01 g/cm^3 (Table 1; Fig. 11).

The stage II-1 calcite also only contains W-type fluid inclusions, which yield final ice-melting temperatures of −20.0 to −5.4 °C (mainly −16.7 to −12.7 °C) with an average of −14.7 °C, constraining a salinity range of 8.5 to 22.4 (main range 16.7–20.1) wt.% NaCl eqv. an average of 18.4 wt.% NaCl eqv. They were homogenized to liquid at 175 to 260 °C (main range 210–260 °C) at an average of 235 °C. Based on the Tm_{ice} and Th_{-tal} of the W-type fluid inclusions, the estimated fluid density is 0.95 to 1.07 g/cm^3 (Table 1; Fig. 11).

The stage II-2–3 calcite contains all four types of fluid inclusions, i.e., W-type (61%), C-type (C1 = 10%; C2 = 7%), S-type (11%) and PC-type (PC1 = 8%; PC2 = 3%). W-type inclusions yielded homogeneous temperatures ranging from 210 to 370 °C (mainly 253–323 °C) with an average of 270 °C, and final ice-

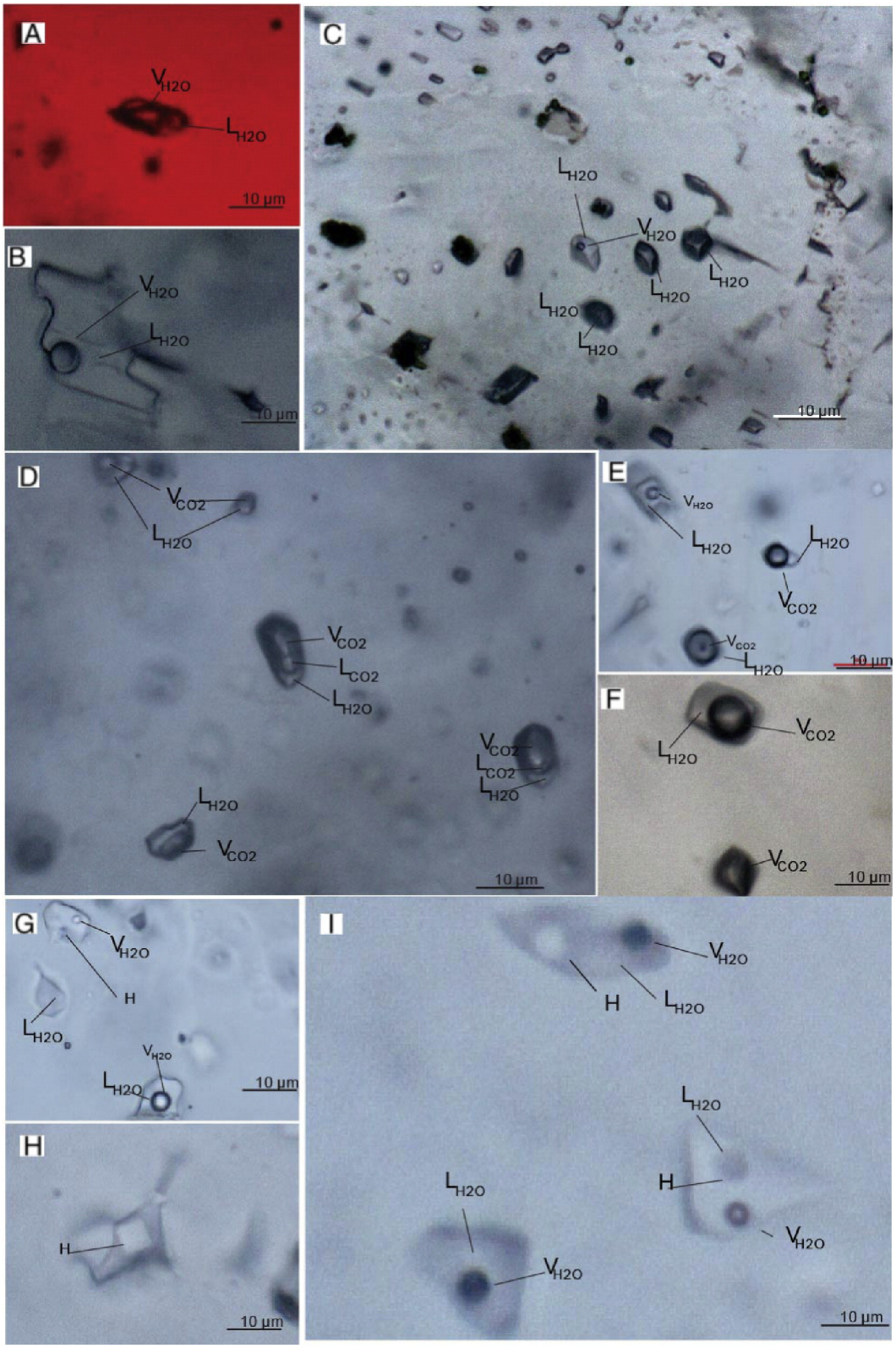

Fig. 10. Fluid inclusion types in the quartz/calcite veins from the Caixiashan deposit (plane-polarized light). A, aqueous (W-type) fluid inclusion in the sphalerite. Sample 13802-45, Zone II. B, W-type fluid inclusions. Sample 13ZKIII-C5, ZK4402 of Zone III. C, W-type fluid inclusions. Sample 13ZKIII-C5, ZK4402 of Zone III. D, carbon phase containing type (C-type) fluid inclusions. Sample 13ZKIV-C7, ZK2901 of Zone IV. E, C-type and W-type fluid inclusions. Sample 13ZKII-C2, ZK003 of Zone I. F, C-type and pure carbon phase (PC-type) fluid inclusions. Sample 13ZKII-C2, ZK003 of Zone II. G, W-type and mineral bearing or multiphase (S-type) fluid inclusions. Sample 13802-45, Zone II. H, S-type fluid inclusion. Sample 13ZKI-14, ZK1602 of Zone I. I, S-type fluid inclusions. Sample 13ZKI-71, ZK1602 of Zone I. Abbreviations: L_{H_2O} = liquid H_2O; V_{H_2O} = vapor H_2O; L_{CO_2} = liquid CO_2; V_{CO_2} = vapor CO_2; H = halite.

melting temperatures are from −21.0 to −3.6 °C with an average of −15.6 °C that correspond to salinities of 5.9 to 23.1 by an average of 19.1 wt.% NaCl eqv. The calculated fluid densities of the W-type fluid inclusions range from 0.72 to 0.99 g/cm^3. Although a few W-type fluid inclusions were identified in the sphalerite (Fig. 10A), no changes were observed during the cooling and

Table 1
Microthermometric data of the fluid inclusions in calcite/quartz from the Caixiashan deposit. Cal = calcite vein; Qtz = quartz vein; N = the number of measured the fluid inclusions; C1 = CO_2 dominant carbon phase containing fluid inclusion; C2 = CH_4 dominant carbon phase containing fluid inclusion; PC1 = CO_2 dominant pure carbon phase fluid inclusion; PC2 = CH_4 dominant pure carbon phase fluid inclusion; Tm_{CO_2} = melting temperature of CO_2; Tm_{clath} = final melting temperature of CO_2–H_2O clathrate; Th_{CO_2} = partial homogenization temperature of CO_2; Tm_{ice} = final melting temperature of ice; Tm_S = final dissolution temperature of halite daughter crystal; Th_{-tal} = total homogenization temperature.

Stage	Host	Type	N	Tm_{CO_2} (°C)	Tm_{clath} (°C)	Th_{CO_2} (°C)	Tm_{ice} (°C)	Tm_S (°C)	Th_{-tal} (°C)	Salinity (wt.%NaCl)	Density (g/cm^3)
I	Cal	W	184	/	/	/	−12.6–0.3 (178)	/	110–236 (181)	0.5–16.5 (178)	0.85–1.01 (178)
II-1	Cal	W	101	/	/	/	−20.0–5.4 (95)		175–260 (97)	8.5–22.4 (95)	0.95–1.07 (96)
II-2–3	Cal	W	61	/	/	/	−21.0−3.6 (60)	/	210–370 (60)	5.9–23.1 (60)	0.72–0.99 (60)
		C1	10	−59.2–56.7 (10)	−5.6–6.6 (9)	7.2–25.2 (5)	/	/	237–371 (10)	6.4–19.7 (9)	1.01–1.06 (5)
		C2	6	/	/	/	/	/	247–345 (6)	/	/
		S	11	/	/	/	/	340–374 (4)	211–350 (11)	42–44 (4)	1.12–1.22 (4)
		PC1	8	−60.0–57.6 (4)	/	7.4–21.2 (4)	/	/	/	/	/
		PC2	3	/	/	/	/	/	/	/	/
III	Qtz	W	53				−20.9–1.0 (52)	/	220–360 (53)	1.7–23.0 (52)	0.81–1.01 (52)
	Cal		45				−17.5–3.4 (45)		225–354 (45)	5.6–20.6 (45)	0.90–1.00 (45)

heating processes. The C1-type inclusions of CO_2 display melting of solid CO_2 at temperatures between −59.2 °C and −56.7 °C with an average of −57.6 °C. The temperatures are slightly lower than the triple point for pure CO_2 (−56.6 °C), indicating the presence of a subordinate amount of other volatiles such as CH_4. Melting of CO_2 clathrate occurs at temperatures between −5.6 °C and 6.6 °C, corresponding to a salinity range of 19.7 and 6.37 wt.% NaCl eqv. Most inclusions show partial homogenization to liquid at temperatures of 7.2 °C to 25.2 °C by average of 19.4 °C. Total homogenization temperatures exhibit a wide range from 237 °C to 371 °C, and their homogenization behavior is dominated by liquid. Some inclusions decrepitate at 350 °C to 425 °C, according to the Tm_{clath}, Th_{CO_2}

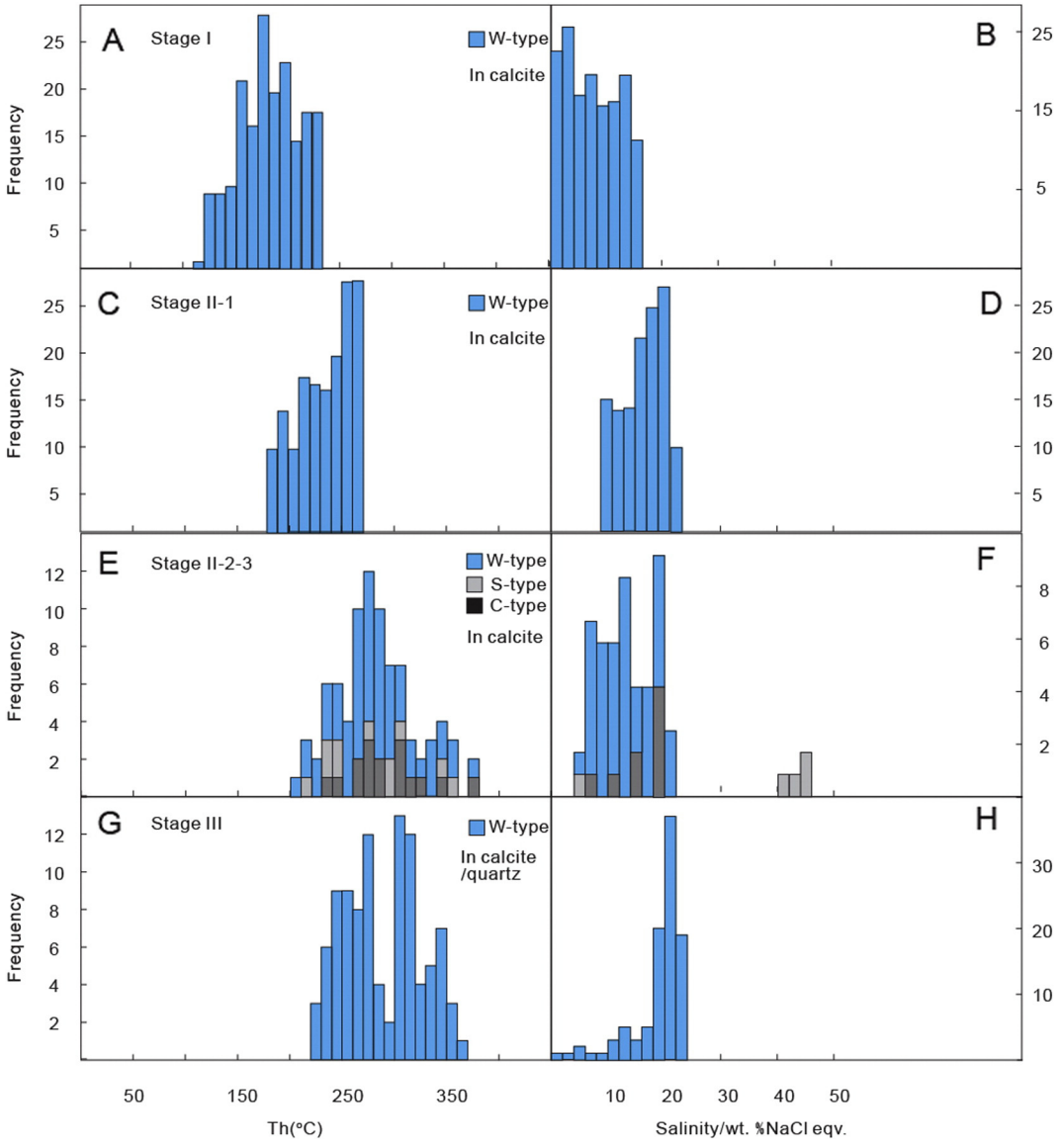

Fig. 11. Histograms of homogenization temperatures and salinities of fluid inclusions in different stages at Caixiashan deposit.

and the estimated volume fraction of CO_2, the estimated fluid density of C1-type ranges from 1.01 to 1.06 g/cm^3. No data was obtained for C2-type of CH_4 as the phase changes at the triple point can be difficult to recognize, the temperature at the triple point (−182.5 °C) is close to the lower limit of commercial stages (*ca.* −196 °C) or solid CH_4 does not always form, but the total homogenization temperatures ranged from 247 to 345 °C. S-type inclusions completely homogenized at temperatures ranging between 211 and 350 °C and dominantly went to vapor. Usually, daughter minerals in the S-type fluid inclusions melted at 340 to 374 °C during heating (Tm_S), indicating a salinity range of 42 to 44 wt.% NaCl eqv. The densities of S-type inclusions of stage II-2–3 are estimated between 1.12 and 1.22 g/cm^3, being the highest densities of all the inclusion types found in this study. The W-type fluid inclusions show a close spatial relationship with the S-type inclusions (Fig. 10G and H), and they share similar homogenization temperatures from 345 to 350 °C, but with different salinities (W-type: 21.0 to 23.1 wt.% NaCl eqv., S-type: 43 to 44 wt.% NaCl eqv.), probably indicating fluid boiling in stage II. The PC1-type inclusions yield melting temperatures for solid CO_2 from −60.0 to −57.6 °C, indicating the presence of other volatiles such as CH_4, which is consistent with the laser Raman spectrum results. The homogenization temperatures of liquid CO_2 and vapor CO_2 to the liquid phase show large variation from 7.4 °C to 21.2 °C with an average of 13.1 °C, for the three PC2-type of fluid inclusions, unfortunately, no change was tracked during the heating and cooling processes as with the C2-type fluid inclusions.

The stage III quartz and calcite contain only W type fluid inclusions. The W-type fluid inclusions in quartz and calcite yielded homogenization temperatures ranging from 220 to 360 °C and 225 to 354 °C, respectively. The final ice-melting temperatures are between −20.9 to −1.0 °C and −17.5 to −3.4 °C corresponding to salinities of 1.7 to 23.0 and 5.6 to 20.6, respectively. Based on the Tm_{ice} and Th_{-tal} of the W-type fluid inclusions, the estimated fluid density is 0.81 to 1.01 (quartz) and 0.90 to 1.00 g/cm^3 (calcite; Table 1; Fig. 11).

4.4. Fluid compositions

As measured by laser Raman microspectroscopy, the vapor bubbles of the C1- (CO_2 dominant), C2- (CH_4 dominant), PC1- (CO_2 dominant),

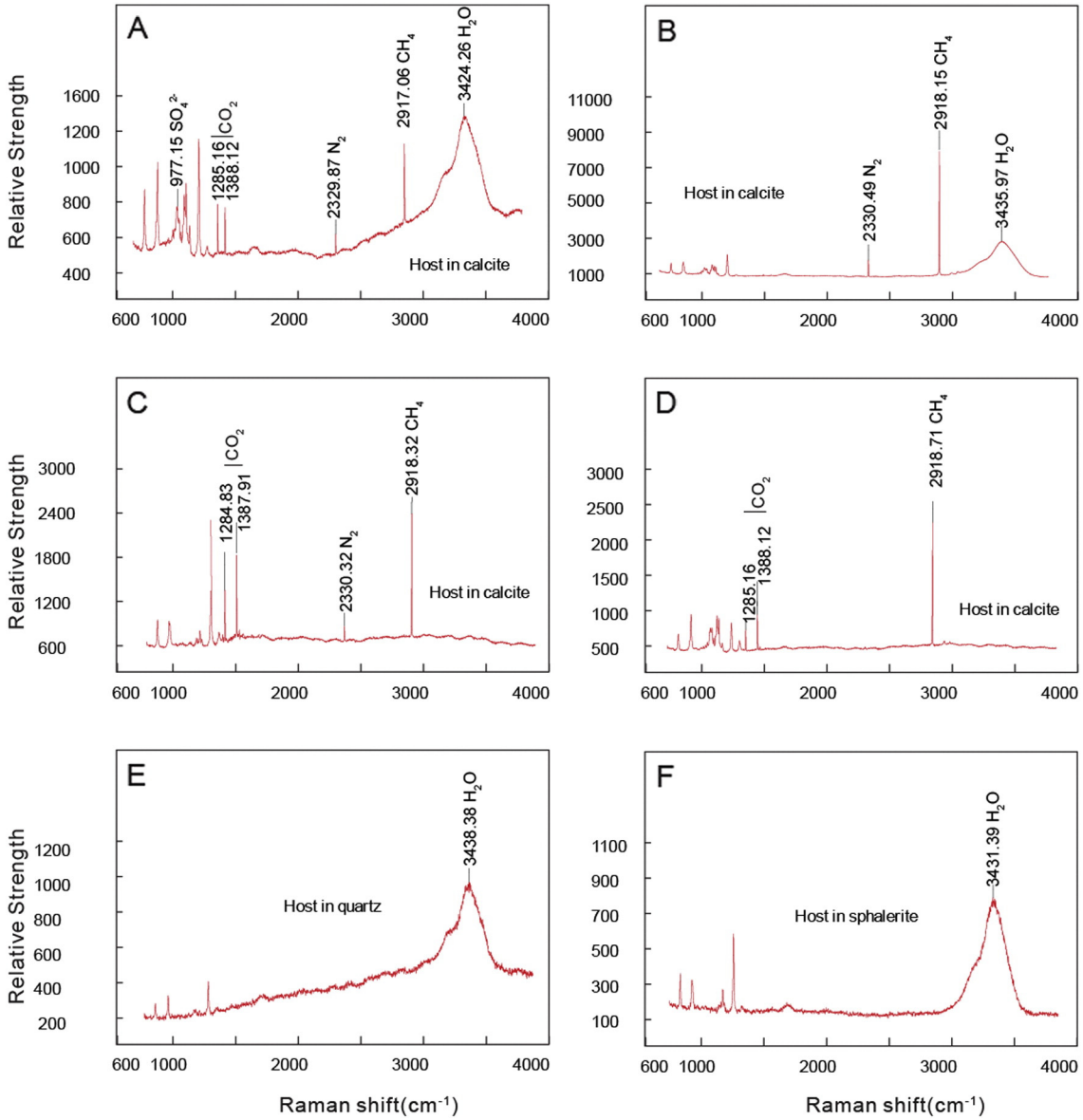

Fig. 12. The LRM spectra of vapor component in fluid inclusion at Caixiashan deposit, A, the C1-type fluid inclusion (CO_2 dominant) coexisting with SO_4^{2-}, N_2, CH_4 and H_2O. B, the C2-type fluid inclusion (CH_4 dominant), also contains H_2O and N_2. C, the PC1-type (CO_2 dominant) fluid inclusion coexisting with N_2 and CH_4. D, the PC2-type (CH_4 dominant) fluid inclusion coexisting with CO_2. E and F show the component of W-type fluid inclusions.

PC2- (CH_4 dominant) and W-type inclusions are shown in Fig. 13. The C1-type fluid inclusions are dominated by a CO_2 vapor component with small amounts of N_2 and CH_4, and the liquid dominated by H_2O and SO_4^{2-} (Fig. 12A). The C2 fluid inclusions are dominated by a CH_4 vapor component with small amounts of N_2, whereas the CO_2 is absent (Fig. 12B). The PC1 fluid inclusions contain local CO_2 and CH_4 with small amounts of N_2 but no H_2O component (Fig. 12C), and the PC2-type fluid inclusions contain more CH_4 than CO_2 with small amounts of N_2 but no H_2O component (Fig. 12D) The W-type fluid inclusions contain relatively high intensity water peaks (Figs. 12E and F). In general, fluid inclusions in Stages I, II-1 and III are dominated by water with no CO_2, whereas Stage II-2–3 is complex and has variable $CO_2 + H_2O \pm N_2 \pm CH_4 \pm SO_4^{2-}$.

5. Discussion

5.1. The reliability of fluid inclusion data

The reliability of fluid inclusion data should be tested to see if fluid inclusions have maintained integrity since their time of formation (Roedder and Ribbe, 1984). Overheating, reequilibration toward lower density (greater inclusion volume) by plastic stretching, or partial leakage of inclusions can all result in anomalously high homogenization temperature values and an overestimate of ore fluid temperatures (Wilkinson, 2010).

However, research shows that the potential for inclusion reequilibration during overheating is largely a function of inclusion size and host mineral strength (Wilkinson, 2010 and references therein). The plot of fluid inclusion size (maximum dimension) against homogenization temperature is useful to evaluate the effects of regional deformation/heating. If partial reequilibration has occurred the fluid inclusions should show a positive correlation, with the effect being more pronounced for softer minerals in which inclusions can deform under lower internal overpressures (e.g., calcite, barite). When applied to the data from Caixiashan, no positive correlation is apparent for the calcite from stage II-2–3, (Fig. 13), and therefore the calculated homogenization temperatures are considered to be reliable.

5.2. Pressure conditions and depth of ore formation

Using the FLINCOR program (Brown, 1989) and $H_{OKIE}F_{LINCS}\_H_2O\text{-}N_AC_L$ program (Steele-MacInnis et al., 2012), the minimum pressure estimates of the hypogene stages range from 0.1 to 2.0 MPa (stage I), 0.9 to 4 MPa (stage II-1), 1.9 to 17.4 MPa (stage II-2–3) and 2.0 to 15.6 MPa (stage III) according to the W- and S-type fluid inclusions, whereas for the C1 fluid inclusions (stage II-2–3), the lowest estimated pressures

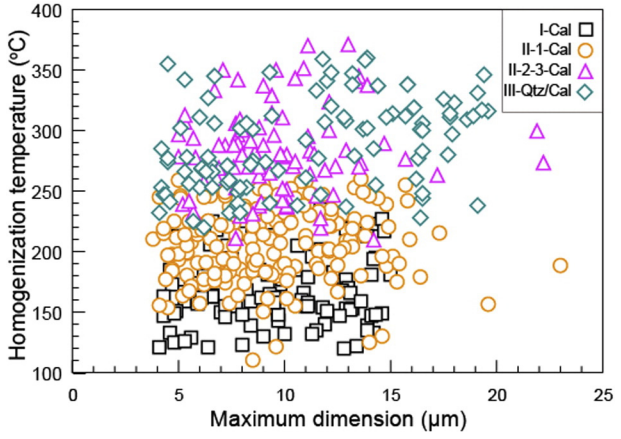

Fig. 13. Plot of homogenization temperature as a function of maximum inclusion dimension for Caixiashan.

are from 9.8 to 22.7 MPa. The burial depth of the Caixiashan can be calculated based on the approximate rock density (2.8 g/cm^3) and lithostatic pressure (28 MPa/km) with the estimated depth of formation of stages I, II-1, II-2–3 and III varying from <0.01–0.07 km, 0.03–0.14 km, 0.07–0.62 km (W/S-type) or 0.35–0.85 km (C1-type) and 0.07–0.55 km, respectively. Alternatively, based on water density (1.0 g/cm^3) and hydrostatic pressure (10 MPa/km), the estimated depth of formation of each stage ranges from 0.01–0.20 km, 0.09–0.40 km, 0.19–1.74 km (W/S-type) or 0.98–2.27 km (C1-type) and 0.20–1.56 km, respectively.

Stage I inclusions are characterized by lower pressures and less gas components, suggesting that they formed close to the surface (<0.1 km) either under the lithostatic or hydrostatic pressure, which indicates that pyrite and coexisting carbonates were formed in an open environment connected directly to the water/atmosphere, consistent with their syn-sedimentary origin. Stage II-1 is also characterized by low pressures but they are generally higher than stage I, which suggests that the stage II-1 pyrite may have formed at slightly greater depths (up to 0.4 km). Stage II-2–3 CH_4 and CO_2-bearing fluids with moderate temperature are characterized by a large range in minimum pressures (9.8 to 22.7 MPa), suggesting a greater depth of about 2.27 km or deeper under purely hydrostatic pressure conditions, or 0.85 km under the lithostatic pressure as a conservative estimate. The syn-sedimentary normal fault systems developed in the Caixiashan district are likely associated with the nearly vertical distribution of the Zn–Pb ore bodies, which suggests that the ore-forming system may have been connected to the surface. Therefore an estimate based on hydrostatic conditions may be applicable for stage II-2–3 ore-forming fluids, indicating that sphalerite precipitation occurred at a depth of around 2 km or shallower, deeper than stages I and II-1. The estimate depth of stage III is about 0.20–1.56 km (hydrostatic) or 0.07–0.55 km (lithostatic) suggesting that the magmatic/metamorphic reworking stage was also close to the surface but possibly occurred at shallower than stage II.

5.3. Evolution of the ore-forming fluids

5.3.1. Formation of sedimentary pyrite of stage I

The stage I colloform/framboidal pyrite (pyrite 1; Fig. 5A–D) may have precipitated at the same time as the sediment, as this texture is typical of pyrite formed in sedimentary environments (Graham et al., 2012). The large volume of pyrite associated with stage I suggests that before precipitation the Fe–S system existed in oxidized conditions, allowing abundant Fe–S-rich fluids to be carried to the site of deposition. Then bacterial reduction would cause the regime to shift to reduce conditions causing the precipitation of pyrite (Butler and Rickard, 2000).

The processes of sedimentary pyrite formation have been well-studied and include bacterial sulfate reduction, reaction of H_2S with iron minerals to form Fe monosulfides, and the reaction of Fe monosulfides with elemental sulfur to form pyrite (Berner, 1970), which will generate very low $\delta^{34}S_{V\text{-}CDT}$ values as noted in Caixiashan with low value as −10.1‰ of pyrite (Gao et al., 2007) or −21.1‰ of pyrite (Cao et al., 2013). The precipitation of pyrite eventually ceased possibly due to a limited supply of H_2S/HS^-. The lack of H_2S/HS^- in a normal marine fluid could result from either inactivity of bacteria or the absence of organic matter (Berner et al., 1985). As no CH_4 was detected in stage I fluid inclusions this suggests that the absence of organic material, was the cause of the decreasing in H_2S/HS^- concentrations.

The initial fluid from stage I is dominated by a H_2O–NaCl (possibly with SO_4^{2-}) brine, with homogenization temperatures and salinity ranging from 110 to 236 °C and 0.5 to 16.5 wt.% NaCl eqv. (Fig. 14A). Some of the fluid temperatures in stage I are slightly higher than the typical for sediment deposition (<200 °C) and those fluids could be responsible for the sedimentary pyrite lens (including colloform and

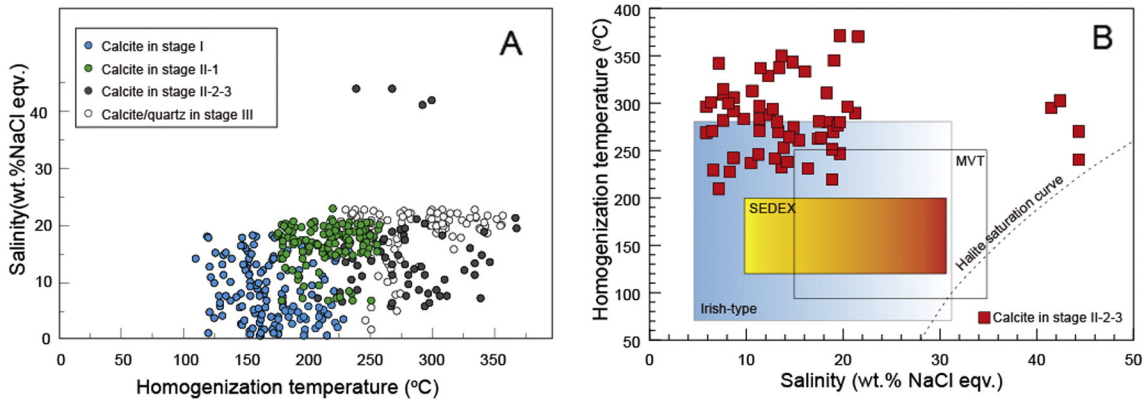

Fig. 14. Evolution of ore-forming fluid. A, the fluid homogenization temperature vs. salinity of each stage at Caixiashan deposit. B, the comparison of Caixiashan with Irish-type and MVT deposit (Wilkinson, 2010).

framboidal pyrite) found within the strata, whereas hotter fluids (>200 °C) may be derived from channelized high-T fluid flow indicated by the calcite of stage I (Almodóvar et al., 1997) or overprinting by later hotter fluids (see below discussion).

5.3.2. Mineralization and associated ore-forming fluids of stage II

The layered pyrite (stage II-1; pyrite 2; Fig. 5E–G) formed later than the pyrite 1 based on: 1) pyrite 2 is spatially associated with recrystallized calcite and dolomite not the host rocks; 2) the pyrite 2 texture is obviously different from the syn-sedimentary pyrite 1 (Fig. 5C and D), and the medium grain size of the co-precipitated calcite and dolomite shows affinity to these typical recrystallized carbonate rocks in stage II; 3) fluid inclusions thermometry (~235 °C) indicate that pyrite 2 formed at relatively higher temperature and greater depths than pyrite 1 (~155 °C); 4) Re–Os dating of pyrite (unpublished data) suggested there is ~200 Ma gap between pyrite 1 and pyrite 2.

The sphalerite (stage II-2) was locally found as pseudomorphs that have replaced stage I colloform pyrite (Figs. 5D and 6F), and formed the massive ore in the Caixiashan deposits. Replacement of pyrite by sphalerite may indicate a reaction process between the ore forming fluid and pyrite when Zn-rich fluids circulated in the system, as supported by the dark brown color of sphalerite in the hand samples or thin sections, which is a signature of Fe-rich sphalerite (Fig. 6B).

That the ore system is dominated by sphalerite rather than galena may be due to 1) the host rock in the Kawabulake Group being enriched in Zn and Fe relative to Pb, or 2) because the ore-forming fluids contained higher contents of Zn. The first reason can be excluded because the dolomitized marble at Caixiashan is enriched in both Zn and Pb and there is no significant difference in the abundance of the two elements (Liang et al., 2008; Peng et al., 2007). Experimental work has suggested that the Zn concentration in acidic solutions is 2–3 orders of magnitude higher than the Pb concentration over broad ranges of temperature, pressure, and Cl concentrations, and that Zn sulfate dissolves more readily than Pb sulfate (Lukanin et al., 2013). Therefore, the ore-forming fluid was initially dominated by Zn–Fe–S with trace Pb, and the pyrite precipitated first due to the lower solubility of Fe as the prior formation of the pyrite 2 of stage II-1. The Fe-rich sphalerite ($Zn_{1-x}Fe_xS$) occurs throughout stage II-2. Research shows that the Fe-rich sphalerite is corresponding to the effect of Fe-substitution of the pyrite (Kharbish, 2007), which means the Fe in the pyrite 2 could also be replaced by Zn and formed Fe-rich sphalerite, which is consistent with some of the observed replacement textures (Fig. 6E and F). Although Fe can commonly substitute in sphalerite, galena can only precipitate with pyrite if extra Fe is present in fluids, which is consistent with our observation of only galena in stage II-3. In general, the Caixiashan deposit is dominated by sphalerite likely due to the higher concentration of Zn than Pb in the ore-forming fluid. Some carbonate-hosted Pb–Zn deposits in the Southeast Missouri district are also Zn rich relative to Pb and have Zn/(Zn + Pb) ratios greater than 0.5 (Leach et al., 2005).

The homogenization temperatures of the main mineralization stage II-2–3 (W-type: 210 to 370 °C with mode of 270 °C; C-type: 237 to 371 °C and S-type: 211 to 350 °C) are generally higher than those typical of MVT deposits (50 to 250 °C; Leach et al., 2005) and more similar to the high-temperature carbonate-hosted deposit in the Irish type ore systems (Fig. 14B), some of which have peak temperature of ~280 °C (Wilkinson, 2010). The high temperatures at Caixiashan are also similar to carbonate-replacement and vein-type deposits of the Christiana replacement deposit in Greece with reported homogenization temperatures of 312 to 399 °C (Voudouris et al., 2008), the carbonate-hosted Kabwe, Tsumeb and Kipushi Pb–Zn–Cu deposits (in Central Africa) with homogenization temperatures from 257 to 385 °C (Kamona et al., 1999) and the carbonate-hosted Ag–Pb–Zn(Cu) deposits of northern Mexico with temperature ranging from 200 to 500 °C (Megaw et al., 1988). The ore-forming fluid (stage II) is preserved in abundant PC- and C-type inclusions. The high concentrations of CH_4, CO_2 coexisting with SO_4^{2-}, in a relatively high-salinity fluid may indicate a complex ore-forming system induced by either fluid mixing or fluid/rock reactions. Thus, the ore-forming fluids at Caixiashan evolved from stage I with depletion of gas components to enrichment in CH_4, CO_2 and N_2 in stage II, with higher salinities and temperatures (Fig. 14A). The increasing salinity could have resulted from dissolution of the sediment, and the increasing homogenization temperature possibly resulted from the collapse of host rocks leading to deep burial as suggested by collapse texture of pyrite (Fig. 7E) and the possible connection with a deeper heat source. The possible boiling fluid inclusions (Fig. 10G and H) imply that the fluid boiling/immiscibility may correspond to the high temperatures and salinities and play an important role in the precipitation of the ore-forming minerals. The discharge of metals in sediments will lead to the release and accumulation of hydrogen ions to generate acidic fluids (Leach et al., 2005), which would eventually accelerate the dissolving of sedimentary rocks and provide more space for sulfide deposition, as evidenced by some of the CO_2 tracked in the fluid inclusion (Fig. 12A, C and D). Host-rock dissolution during the deposition of metal in MVT and other carbonate-hosted deposits has been widely documented, as the dissolution and hydrothermal brecciation of the host rocks can be caused by acid-producing reactions commonly associated with fluid mixing (Anderson, 1975; Sverjensky, 1984, 1986). However, it is difficult to maintain these reactions as the gradually stronger acid solution will not only provide the preservation place but also dissolve the sulfides formed earlier.

Based on field observations, dolomitized marble is closely associated with the mineralization at Caixiashan deposits and the sulfide ore bodies are broadly coeval with dolomitic alteration (Fig. 4). The well-developed dolomitic alteration at Caixiashan may have formed

a natural barrier that isolated the Pb and Zn minerals from the acidic fluids.

The coexistence of CH_4 and SO_4^{2-} in fluid inclusions was identified in the main mineralization stage (stage II-2–3; Fig. 12A). Research shows that the lowest temperature for the CH_4 reactions with sulfate (or SO_4^{2-}) to be as low as ~100 °C (Zhu et al., 2005), which will generate H_2S for sulfide precipitation. The HS^- is interpreted to have been generated during the reduction process, which would be characterized by light sulfur as a result of isotopic fractionation. However, most of the sulfides at Caixiashan are characterized by heavy sulfur isotopic compositions ($\delta^{34}S_{V\text{-}CDT}$ of pyrite as much as 19.1; Gao et al., 2007; Cao et al., 2013), which suggests that the methane or other organic matter might entirely convert the sulfur in the sulfate, or that the ore-forming fluids are originally derived from basinal brines that were characterized by heavy sulfur, suggesting the initial ore-forming fluid is oxidized.

5.3.3. The magmatic/metamorphic reworking process of stage III

Tremolitization overprinting the sulfide ores may be associated with the magmatism around the Caixiashan ore district (Fig. 3). The magmatic/metamorphic fluids caused hydrothermal alteration in the host rock and remobilized the sulfide and formed sphalerite as a result of fluid-sulfide/host rock interaction. Even though the magmatic/metamorphic fluid should modify the trace element and the isotope compositions, there seems to be no significant contribution to the ore grade and reserves.

The homogenization temperature and salinity of stage III are concentrated around 311 °C and 20.1 wt.% NaCl eqv., respectively. The fluids associated with the magmatic/metamorphic reworking stage show higher modal homogenization temperatures and salinity than stage II (Fig. 14A), which is consistent with a magmatic/metamorphic origin for stage III, although the genetic connection of stage II fluids with magmatism cannot be excluded. However, fewer sulfides were precipitated in stage III possibly because of the depletion of reducing agent (CH_4), or simply due to low concentration of metals in the fluids.

5.4. Metallogenesis and ore deposit modeling

As shown in Table 2, the Caixiashan Zn–Pb deposit appears to be similar to sedimentary-hosted base metal deposits to varying degrees, but it also has some distinct features. Caixiashan is likely not a SEDEX deposit for three reasons: 1) SEDEX deposits are usually syngenetic, but geological and petrographic evidences show that the Caixiashan is formed by carbonate replacement and dissolution, consistent with an epigenetic deposit; 2) SEDEX deposits are usually hosted by the clastic-dominated rocks, whereas the mineralization at Caixiashan is closely related to a carbonate-dominated sequence; and 3) the ores in SEDEX deposit are typically fine-grained, laminated and stratiform, but at Caixiashan, vein type ore is more apparent than the stratiform.

Caixiashan does not resemble a traditional MVT deposit as the fluid inclusion evidence shows that fluid temperatures are generally higher than those of typical MVT deposit (50 to 250 °C; Leach et al., 2005) and the high updip vein-type ore is more apparent than the fine-grained banded ore. Furthermore, unlike orogenic-related MVT deposits, Caixiashan is hosted in an extensional basin with the early stage of Caixiashan mineralization including synsedimentary sulfides related to normal faults. All of these suggest that Caixiashan is not an orogenic-related MVT deposit. Caixiashan shares many similarities with the Irish-type Zn–Pb deposits (Table 2), including the geology, fluid inclusion and sulfur isotopes, similar tectonic setting, carbonate-dominated host rocks and similarities in alteration and mineralizing type. Moreover, the fluid inclusion homogenization temperature and salinity are similar to the high-temperature carbonate-hosted deposit in Irish ore field (Fig. 14B), with highest Th concentrated around ~280 °C and salinity varies from 4 to 31 wt.% NaCl eqv. (Wilkinson, 2010).

We propose the following genetic model for the Caixiashan Pb–Zn deposit. In the relatively stable passive margin environment, downwards flow circulation will leach Fe from the sediments and bring the sulfate-containing fluid into recharge zone, and then they were reduced by bacteria and precipitated abundant pyrite (Fig. 15A). The activities of the normal faults reopened the system and accelerated the reaction between Cl^- and SO_4^{2-}-rich marine (or basin brine) with the metal-rich sediment, resulting in high concentrations of Zn, Fe and Pb chloride or sulfate in the ore-forming fluids, which were then buried during basinal collapse. Meanwhile the CH_4 in the carbonate rocks was released into the system resulting in the discharge of Zn–Pb ores by thermal sulfate reduction at a relatively higher temperature of 270 °C (Fig. 15B). Those massive sulfides appear to have precipitated from an ore-forming fluid that was oversaturated with metals (Zn, Fe and Pb) at the beginning of the thermal sulfate reduction, as suggested by some of the S-type fluid inclusions. During the Late Paleozoic, as a result of the closure of Paleoasian Ocean, widespread of arc magmatism developed in the Caixiashan area and generated intensive high-temperature hydrothermal tremolite and quartz alteration overlapping on the Caixiashan Zn–Pb ore bodies, resulting in remobilization of some minerals such as sphalerite (Fig. 15C).

Table 2
Comparison between the Caixiashan, the SEDEX, MVT and Irish-type Zn–Pb deposit.

Deposit type	Caixiashan	SEDEX (Leach et al., 2005)	MVT (Leach et al., 2005)	Irish-type (MVT subtype) (Wilkinson et al., 2005)
Tectonic setting	Passive margin and extensional environment.	Passive margins and continental rift-sag basins	Passive margin environments and commonly related to extensional domains	Passive margin environments and extensional domains
Host rock	Carbonate-dominated: Carbonate rocks, limestone, dolomite-marble.	Clastic-dominated: variety of host rocks: shale, carbonate, coarse clastics	Carbonate-dominated: dolostone and limestone, rarely in sandstone	Carbonate-dominated: carbonate rocks
Metallogenesis	Epigenetic	Syngenetic	Epigenetic	Epigenetic
Ore mineral	Abundant Sp, Gn, Py and Po, minor Apy and Ccp	Py, Po, Sp, Gn, Ccp, trace Apy, Mgt and Td.	Sp, Gn, Py and Mrc	Abundant Sp, Gn and Py, less Mrc, minor Ccp and Tn
Gangue mineral	Cal, Dol and minor Qtz	Qtz, Cal, Brt, Chl, Mus	Dol, Cal, minor Brt and rare Fl	Dol, Brt, Cal and minor Qtz
Alteration	Dolomitization, carbonation, silicification	Silicification, tourmalinization, sericitization, chloritization	Dolomitization, host-rock dissolution, and brecciation	Dolomitization, carbonation
Mineralizing type	Vein, massive and less as stratiform	Typical fine-grained, laminated and stratiform	Replacement of carbonate rocks and to a lesser extent, open-space fill	A variety of massive, disseminated, breccia- and vein filling
Fluid inclusions	210 to 370 °C and concentrated around 270 °C	~10 to 30 wt.% NaCl eqv., 120 to 200 °C and concentrated around 225 °C	~10 to 35 wt.% NaCl eqv., 50 °C to about 250 °C	~4 to 31 wt.% NaCl eqv., 70 to 280 °C, some of them even concentrated around 280 °C
$\delta^{34}S_{V\text{-}CDT}$ (‰)	−21.1 to 19.1	−7.5 to 34.1	−30.0 to 35.0	−44.1 to 11.8

Abbreviations, Py = pyrite; Sp = sphalerite, Dol = dolomite, Cal = calcite, Gn = galena, Po = pyrrhotite, Qtz = quartz, Tr = tremolite, Apy = arsenopyrite, Brt = barite, Fl = fluorite, Td = tetrahedrite, Tn = Tennantite, Mrc = marcasite, Mgt = magnetite.

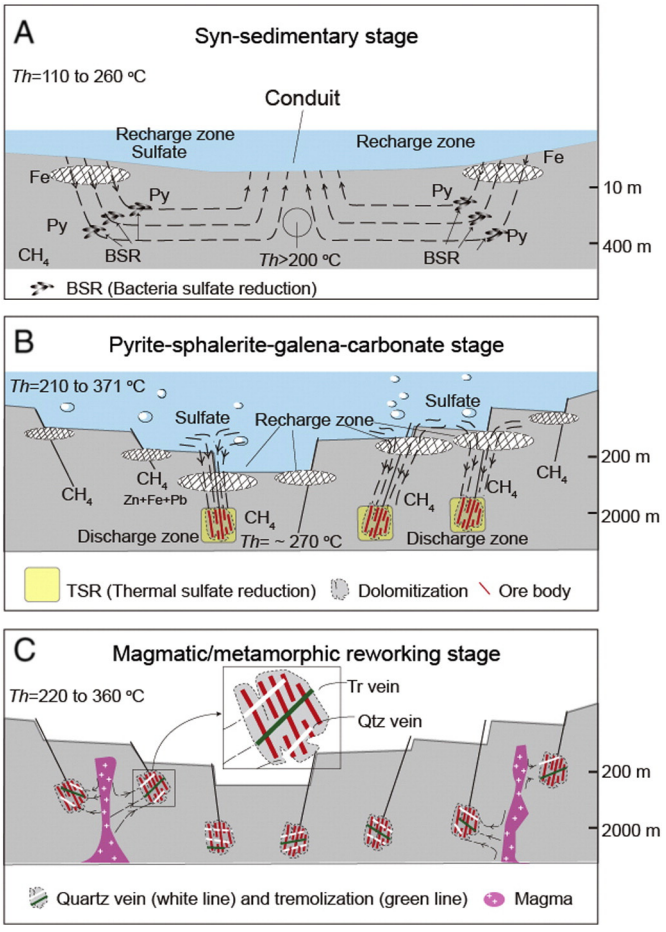

Fig. 15. Genetic model for mineralization of each stage (I to III) in the Caixiashan carbonate-hosted deposit.

6. Conclusions

Three fundamental mineralization stages are recognized at the Caixiashan deposit based on the mineral assemblages and textures, i.e., syn-sedimentary pyrite stage, the main mineralization stage and the magmatic/metamorphic reworking stage. The syn-sedimentary pyrite stage formed in a shallow sedimentary environment, with average homogenization temperatures and salinities around 168 °C and 10.1 wt.% NaCl eqv.. The main mineralization occurred at greater depths as a result of thermal sulfate reduction, as evidenced by CH_4 and SO_4^{2-} in the fluid inclusions, and the homogenization temperature around 270 °C that would have maintained the reduction. Fluid flow was focused on fracture zones associated with the main Caixiashan extensional faults. The dolomite subsequently precipitated from the high temperature hydrothermal fluids in hydraulic fractures and breccias as the system became sealed. The magmatic hydrothermal alteration overprinted the orebodies but made only a minor contribution to the mineralization, suggesting that the ore forming fluids were probably derived from heated Precambrian basinal brines, rather than the Late Paleozoic magmatic hydrothermal fluids. This main ore-forming process is consistent with geologic and geochemical evidence from the other economic carbonate-hosted deposits.

Conflict of interest

We wish to confirm that there are no known conflicts of interest associated with this publication and there has been no significant financial support for this work that could have influenced its outcome.

Acknowledgments

This study was financial supported by the Chinese National Basic Research 973-Program (2014CB440802), the Geological Survey of China (Project 1212011140056), the Creative and interdisciplinary program, CAS (Y433131A07), the NSFC (nos. 41072062, 41472077 and 40730421) and the China Scholarship Council Fund (201404910423). The Office of Project-305, the First Brigade of Xinjiang Geology and Mineral Resources Bureau of Xinjiang Institute of Geological Survey helped our field investigation. The master students Emily Smyk, Michael D' Angelo, Sean Francis O'Brien, Adrian Arts and Chris Yip of Lakehead University kindly help with the English writing. Two anonymous reviewers are thanked for constructive reviews that greatly improved the quality of this paper. This is contribution No. IS-2095 from GIGCAS.

References

Allen, M., Natal'in, B., 1995. Junggar, Turfan and Alakol basins as Late Permian to? Early Triassic extensional structures in a sinistral shear zone in the Altaid orogenic collage, Central Asia. J. Geol. Soc. 152, 327–338.
Almodóvar, G.R., Sáez, R., Pons, J.M., Maestre, A., Toscano, M., Pascual, E., 1997. Geology and genesis of the Aznalcóllar massive sulphide deposits, Iberian Pyrite Belt, Spain. Mineral. Depos. 33, 111–136.
Anderson, G., 1975. Precipitation of Mississippi Valley-type ores. Econ. Geol. 70, 937–942.
Appold, M.S., Wenz, Z.J., 2011. Composition of ore fluid inclusions from the Viburnum Trend, Southeast Missouri district, United States: implications for transport and precipitation mechanisms. Econ. Geol. 106, 55–78.
Berner, R.A., 1970. Sedimentary pyrite formation. Am. J. Sci. 268, 1–23.
Berner, R.A., Leeuw, J.W.D., Spiro, B., Murchison, D.G., Eglinton, G., 1985. Sulphate reduction, organic matter decomposition and pyrite formation [and Discussion]. Philos. Trans. R. Soc. Lond. A Math. Phys. Sci. 315, 25–38.
Bodnar, R.J., 1993. Revised equation and table for determining the freezing point depression of H_2O–NaCl solutions. Geochim. Cosmochim. Acta 57, 683–684 (United States).
Brown, P.E., 1989. Flincor: a microcomputer program fro the reduction adn investigation of fluid-inclusion data. Am. Mineral. 74, 1390–1393.
Butler, I.B., Rickard, D., 2000. Framboidal pyrite formation via the oxidation of iron (II) monosulfide by hydrogen sulphide. Geochim. Cosmochim. Acta 64, 2665–2672.
Cai, X.F., Tian, W.M., Zhang, X.H., Wu, L.Y., 2013. Formation symbols and significance of Mesoproterozoic carbonate platform in the area of Kavabulake, Xinjiang. Resour. Surv. Environ. 34, 8–15 (in Chinese with English abstract).
Cao, X.F., Lv, X.B., Zhang, P., Liu, S.T., Gao, X., Gao, L.Y., Tang, R.K., Wang, Y.J., Hu, Q., 2013. Stable isotope geochemistry and ore genesis of Caixiashan Pb–Zn deposit at eastern Middle Tianshan, Xinjiang. J. Cent. South Univ. (Sci. Technol.) 44, 662–672 (in Chinese with English abstract).
Chen, Y.J., Ni, P., Fan, H.R., Pirajno, F., Lai, Y., Su, W.C., Zhang, H., 2007. Diagnostic fluid inclusions of different types hydrothermal gold deposits. Acta Pet. Sin. 23, 2085–2108 (in Chinese with English abstract).
Collins, P.L., 1979. Gas hydrates in CO_2-bearing fluid inclusions and the use of freezing data for estimation of salinity. Econ. Geol. 74, 1435–1444.
Deng, X., Wang, J., Wang, Y., Li, Y., Fang, T., Mao, S., 2014. Geological Characteristics of the Hongshi Cu–Au Deposit, Eastern Tianshan, Xinjiang and Discussion of the Deposit Genesis Miner Explor. pp. 159–168 (in Chinese with English abstract).
Dong, L.X., 2005. The break up and reassessment of Kawabulake Group in Eastern Tianshan, Xinjiang. Xinjiang Geol. 23, 19–22 (in Chinese with English abstract).
Frezzotti, M.L., Tecce, F., Casagli, A., 2012. Raman spectroscopy for fluid inclusion analysis. J. Geochem. Explor. 112, 1–20.
Gao, X.L., Peng, M.X., Hu, C.A., Wang, D.H., Liang, T., Gao, J.G., 2006. Fluid inclusions of Caixiashan Pb–Zn deposit in Xinjiang. J. Earth Sci. Environ. 28, 25–29 (in Chinese with English abstract).
Gao, J.G., Liang, T., Peng, M.X., Li, Y.L., Wang, L., Gao, X.L., 2007. Sulfur, carbon, hydrogen and oxygen isotope geochemistry of Caixiashan lead–zinc deposit, Xinjiang. Geophys. Prospect. 43, 57–60 (in Chinese with English abstract).
Geological Team 1 of Xinjiang Bureau of Geology and Mineral Resources, 2007. The Evaluation of the Prospected Mineral Resources in Eastern Tianshan, Xinjiang. p. 41 (in Chinese).
Goldstein, R.H., Reynolds, T.J., 1994. Systematic of fluid inclusions in diagenetic materials. Soc. Sediment. Geol. Short Course 31, 199.
Graham, G., Hitzman, M.W., Zieg, J., 2012. geologic setting, sedimentary architecture, and paragenesis of the Mesoproterozoic sediment-hosted sheep creek Cu–Co–Ag deposit, Helena Embayment, Montana. Econ. Geol. 107, 1115–1141.
Herzig, P.M., Hannington, M.D., 1995. Polymetallic massive sulfides at the modern seafloor—a review. Ore Geol. Rev. 10, 95–115.
Kamona, A.F., Leveque, J., Friedrich, G., Haack, U., 1999. Lead isotopes of the carbonate-hosted Kabwe, Tsumeb, and Kipushi Pb–Zn–Cu sulphide deposits in relation to Pan African orogenesis in the Damaran-Lufilian fold belt of Central Africa. Mineral. Depos. 34, 273–283.
Kharbish, S., 2007. A Raman spectroscopic investigation of Fe-rich sphalerite: effect of fe-substitution. Phys. Chem. Miner. 34, 551–558.

Kucha, H., Schroll, E., Raith, J., Halas, S., 2010. Microbial sphalerite formation in carbonate-hosted Zn–Pb ores, Bleiberg, Austria: micro-to nanotextural and sulfur isotope evidence. Econ. Geol. 105, 1005–1023.
Leach, D., Sangster, D., Kelley, K., Large, R.R., Garven, G., Allen, C., Gutzmer, J., Walters, S., 2005. Sediment-hosted lead–zinc deposits: a global perspective. Econ. Geol. 100, 561–607.
Liang, T., Wang, D.H., Hu, C.A., Peng, M.X., Wang, C.L., Gao, X.L., 2008. Geochemistry of trace and REE elements in the Caixiashan Pb–Zn deposit, Xinjiang. Geophys. Prospect. 44, 1–9 (in Chinese with English abstract).
Lukanin, O., Ryzhenko, B., Kurovskaya, N., 2013. Zn and Pb solubility and speciation in aqueous chloride fluids at T–P parameters corresponding to granitoid magma degassing and crystallization. Geochem. Int. 51, 802–830.
Megaw, P.K.M., Ruiz, J., Titley, S.R., 1988. High-temperature, carbonate-hosted Ag–Pb–Zn (Cu) deposits of northern Mexico. Econ. Geol. 83, 1856–1885.
Peng, M.X., Wang, J.L., Yu, W.Y., Zhang, Z., Zhang, T., Wang, W.J., 2007. Geological characteristics features and building about respexting-model of the Caixiashan lead–zinc deposit in the Shanshan, Xinjiang. Xinjiang Geol. 24, 405–411 (in Chinese with English abstract).
Peng, M.X., Sang, S.J., Zhu, C., Chen, J., Wu, L.B., Liang, T., Wu, X.J., Wu, H.P., 2008. Forming analysis of the Caixiashan lead–zinc deposit Xinjiang and comparison with the MVT deposit. Xinjiang Geol. 25, 373–378 (in Chinese with English abstract).
Pirajno, F., Mao, J., Zhang, Z., Zhang, Z., Chai, F., 2008. The association of mafic–ultramafic intrusions and A-type magmatism in the Tian Shan and Altay orogens, NW China: implications for geodynamic evolution and potential for the discovery of new ore deposits. J. Asia Earth Sci. 32, 165–183.
Roedder, Edwin, Ribbe, P.H., 1984. Fluid inclusions. Rev. Mineral. 12, 644–645.
Steele-MacInnis, M., Lecumberri-Sanchez, P., Bodnar, R.J., 2012. HokieFlincs_H_2O-NaCl: a Microsoft Excel spreadsheet for interpreting microthermometric data from fluid inclusions based on the PVTX properties of H_2O–NaCl. Comput. Geosci. 49, 334–337.
Sun, L., Xiao, K.Y., Gao, Y., 2013. Primary Holos characteristics of Caixiashan Pb–Zn deposit and prediction for deep mineralization. J. Jilin Univ. (Earth Sci. Ed.) 43, 1179–1189.
Sverjensky, D.A., 1984. Oil field brines as ore-forming solutions. Econ. Geol. 79, 23–37 (in Chinese with English abstract).
Sverjensky, D.A., 1986. Genesis of Mississippi Valley-type lead–zinc deposits. Annu. Rev. Earth Planet. Sci. 14, 177–199.
Tang, G.J., Wang, Q., Wyman, D.A., Li, Z.X., Zhao, Z.H., 2012. Late Carboniferous high εNd (t)–εHf(t) granitoids, enclaves and dikes in western Junggar, NW China: ridge-subduction-related magmatism and crustal growth. Lithos 140, 86–102.
Vityk, M.O., Bodnar, R.J., Schmidt, C.S., 1994. Fluid inclusions as tectonothermobarometers: relation between pressure–temperature history and reequilibration morphology during crustal thickening. Geology 22, 731–734.
Voudouris, P., Melfos, V., Spry, P.G., Bonsall, T.A., Tarkian, M., Solomos, C., 2008. Carbonate-replacement Pb–Zn–Ag ± Au mineralization in the Kamariza area, Lavrion, Greece: mineralogy and thermochemical conditions of formation. Mineral. Petrol. 94, 85–106.
Wilkinson, J.J., 2010. A review of fluid inclusion constraints on mineralization in the Irish ore field and implications for the genesis of sediment-hosted Zn–Pb deposits. Econ. Geol. 105, 417–442.
Wilkinson, J.J., Eyre, S.L., Boyce, A.J., 2005. Ore-forming processes in Irish-type carbonate-hosted Zn–Pb deposits: evidence from mineralogy, chemistry, and isotopic composition of sulfides at the Lisheen mine. Econ. Geol. 100, 63–86.
Xia, L., Xia, Z., Xu, X., Li, X., Ma, Z., 2012. Mid–Late Neoproterozoic rift-related volcanic rocks in China: geological records of rifting and break-up of Rodinia. Geosci. Front. 3, 375–399.
Xiao, W., Kröner, A., Windley, B., 2009. Geodynamic evolution of Central Asia in the Paleozoic and Mesozoic. Int. J. Earth Sci. 98, 1185–1188.
Xiu, Q.Y., Fei, Y.H., Quan, L., 2002. A single zircon U–Pb age for the granodiorite of Kawabulake complex, Xinjiang, China. Xinjiang Geol. 20, 335–337 (in Chinese with English abstract).
Yin, J., Yuan, C., Sun, M., Long, X., Zhao, G., Wong, K.P., 2010. Late Carboniferous high-Mg dioritic dikes in Western Junggar, NW China: geochemical features, petrogenesis and tectonic implications. Gondwana Res. 17, 145–152.
Zheng, B., Zhu, W., Jahn, B.M., Shu, L., Zhang, Z., Su, J., 2010. Subducted Precambrian oceanic crust: geochemical and Sr–Nd isotopic evidence from metabasalts of the Aksu blueschist, NW China. J. Geol. Soc. 167, 1161–1170.
Zhu, G.Y., Zhang, S.C., Liang, Y.B., Dai, J.X., Li, J., 2005. Alteration of thermochemical sulfate reduction to hydrocarbons. Acta Pet. Sin. 26, 48–52 (in Chinese with English abstract).